Applied Thermal Engineering 278 (2025) 127183

Contents lists available at ScienceDirect

Applied Thermal Engineering

journal homepage: www.elsevier.com/locate/apthermeng

Research Paper

Numerical analysis of copper foam-enhanced hybrid battery thermal management systems for lithium-ion batteries: advancing energy density and thermal control

Alireza Keyhani-Asl, Noel Perera [*], Jens Lahr, Reaz Hasan

College of Engineering, Faculty of Computing, Engineering and the Built Environment, Birmingham City University, Birmingham B4 7XG, UK

ARTICLE INFO

Keywords:
Hybrid battery thermal management system
Energy density
Lithium-ion battery
Phase change material
Copper foam
Cooling plates

ABSTRACT

With the growing demand for efficient and safe energy storage solutions, this study explores the effective and optimised integration of copper metal foam in hybrid battery thermal management systems (HBTMS). A novel HBTMS design is proposed, combining cooling plates with enhanced liquid cooling by metal foam layers in copper tubes and phase change material (PCM) cooling improved by copper foam longitudinal fins. Numerical simulations were conducted using a lumped-capacitance thermal model for transient battery heat generation, the enthalpy-porosity method for PCM, Darcy-Brinkman-Forchheimer (DBF), local thermal equilibrium (LTE) and non-equilibrium (LTNE) models for metal foam. Unlike previous studies that address passive and active cooling separately, present investigation uniquely integrates copper foam into both domains by enhancing conduction in the PCM and improving convection in the coolant channels. This integrated approach achieves superior thermal control, improved energy density, and ensures operational safety. The system's performance under high 5C discharge rates demonstrated a significant reduction of about 9 K in the maximum battery surface temperature compared to pure PCM cooling while maintaining the maximum battery surface temperature difference below 1 K. The study highlights the optimal copper foam layer thickness of 4 mm, balancing improved heat transfer and minimal pressure drop. Furthermore, the incorporation of the metal foam layers reduced the number of required cooling plates, resulting in an 11 % improvement in energy density.

1. Introduction

In light of increasing concerns about climate change and the carbon footprint of fossil fuels, researchers are actively exploring alternative energy sources to mitigate greenhouse gas emissions [1]. Lithium-ion batteries (LIBs), in particular, have attracted significant interest as one of the most promising alternatives, owing to their exceptional energy efficiency, immunity to memory effect, and low self-discharge, characteristics that make them a dependable option for electrical energy storage [2]. However, the performance of LIBs is highly sensitive to temperature. Under low-temperature conditions, battery efficiency deteriorates, leading to decreased charge acceptance, reduced energy storage capacity, lower power output, and faster degradation [3,4]. Conversely, high temperatures degrade capacity, shorten lifespan, and pose safety risks, including thermal runaway [5,6]. Generally, the optimal operating temperature range for LIBs is between 25 °C and 45 °C [7,8]. Also, it is vital to maintain uniform temperature, keeping the temperature gradient below 5 °C [9–11]. Consequently, employing an effective battery thermal management system (BTMS) is essential to ensure both optimal performance and safety.

Phase change materials (PCM) are capable of absorbing generated heat via latent heat. Since the phase change process occurs at a nearly constant temperature, it can provide a reliable and consistent thermal management approach. A major issue with the application of PCMs is found to be the low thermal conductivity [12–14]. This could be enhanced by the incorporation of metal foams [15]. However, the addition of metal foams will also reduce the volume fraction of pure PCM per unit volume, hence lowering the PCM's latent heat and heat storage capacity. In order to improve the thermal conductivity of the PCM, it is necessary to determine the optimal amount of any additional material [10,16]. Sun et al. [17] conducted an experimental study of BTMS for LG 21,700 NMC811 battery using paraffin and copper foam. They demonstrated that selecting a PCM with higher latent heat improved the cell-to-pack ratio and limited the temperature difference in the battery module to less than 5 °C at 3C discharge rate. Rajan et al.

---

[*] Corresponding author.
E-mail address: noel.perera@bcu.ac.uk (N. Perera).

https://doi.org/10.1016/j.applthermaleng.2025.127183
Received 16 March 2025; Received in revised form 24 May 2025; Accepted 7 June 2025

Nomenclature

A_m	Constant for mushy zone ($kg\cdot m^{-3}\cdot s^{-1}$)
C	Coefficient of inertia
C_0	Battery nominal capacity (Ah)
C_F	Geometric parameter
C_p	Specific heat capacity ($J\cdot kg^{-1}\cdot K^{-1}$)
D	Copper tube diameter (m)
E_d	Energy density ($Wh\cdot kg^{-1}$)
F_s	Safety coefficient
H	Total enthalpy (J)
I	Electric current (A)
K	Permeability of the metal foam (m^2)
L_f	Liquid fraction
N	Total number of grids
$\overline{Nu}$	Nusselt number (average)
P	Pressure (Pa)
p	Convergence rate
Q_t	Total heat generation rate (W)
R_t	Internal resistance (Ω)
T	Temperature (K)
U	Nominal voltage (V)
$\overrightarrow{V}$	Velocity vector ($m\cdot s^{-1}$)
V_i	Volume of each computational cell (m^3)
Y	Dimensionless coordinate
a_{sf}	Specific surface area (m^{-1})
d_f	Ligament diameter (m)
d_p	Pore size (m)
f	Solution value
f_r	Friction factor
$\overrightarrow{g}$	Acceleration due to gravity ($m\cdot s^{-2}$)
h	Sensible enthalpy ($J\cdot kg^{-1}$)
h_f	Latent heat of fusion ($J\cdot kg^{-1}$)
h_{sf}	Solid-fluid heat transfer coefficient ($W\cdot m^{-2}\cdot K^{-1}$)
k	Thermal conductivity ($W\cdot m^{-1}\cdot K^{-1}$)
k_{td}	Coefficient of thermal dispersion ($W\cdot m^{-1}\cdot K^{-1}$)
m	Mass (kg)
q_b	Heat generation per unit volume ($W\cdot m^{-3}$)
r	Ratio of grid refinement
t	Time (s)
ΔP	Pressure drop (Pa)
ΔT	Temperature variation (K)
$\frac{dE}{dT}$	Entropy coefficient ($V\cdot K^{-1}$)

Greek Letters

ω	Pore density (PPI)
β	Thermal expansion coefficient (K^{-1})
ε	Porosity
ε_r	Relative error
μ	Dynamic viscosity (Pa·s)
ρ	Density ($kg\cdot m^{-3}$)
θ	Non-dimensional temperature

Subscripts

Amb	Ambient
b	Battery
eff	Effective
f	Fluid
Max	Maximum
ref	Reference
s	Solid
Sur	Surface
t	Total

[18] and Buonomo et al. [19] employed experimental and numerical approaches to analyse the effects of copper foam. Rajan et al. [18] found that copper foam reduced the maximum temperature of a $LiFePO_4$ battery by 7 °C and achieved a uniform temperature profile, while Buonomo et al. [19] highlighted the role of 40 PPI copper foam in enhancing thermal conductivity over 20 PPI foam. El Idi et al. [20,21] combined experimental and numerical methods to study a BTMS for 18,650 LIBs with paraffin RT27 and aluminium foam. They emphasised the importance of axial thermal conductivity, achieving up to an 11 °C reduction in temperature while maintaining operating temperatures around 25 °C. Lin et al. [22] conducted an experimental study to investigate the thermal management of 18,650 LIBs using a CNT@MXene porous composite PCM system. The study demonstrated that the integration of the porous media significantly improved the thermal conductivity of the PCM, reducing maximum battery temperatures by up to 14.19 °C and lowering the temperature rise rate by 50 % under high C-rate conditions. Additionally, their findings indicated that the system effectively enhanced temperature uniformity, decreased PCM leakage, and extended battery lifespan by 28.13 %, 18.92 %, and 11.83 % under 4C, 3C, and 2C discharge rates, respectively. Li et al. [23] conducted a numerical study on a BTMS using PCM combined with toroidal porous media for cylindrical LIBs, investigating the effects of Rayleigh number, porous structure thickness, and material type. They found that a thickness of 0.273R optimally balanced conduction and convection, and reduced the melting time by up to 24.6 %. At high Rayleigh numbers, excessive convection led to heat accumulation, slowing full PCM melting. Structural configuration had a more significant impact than material type, with scattered porous distributions improving temperature uniformity and latent heat usage.

Liquid cooling offers superior heat transfer rates and enhanced cooling performance compared to PCM-based cooling systems and is widely recognised as the most commonly adopted method in practical applications. It is employed in electric vehicles such as the Chevrolet Volt, Tesla Model S, Tesla Model 3, and BMW i3 and i8 [9]. A critical aspect of liquid cooling system design lies in the configuration of liquid flow channels within cooling plates or jackets. In systems utilising conventional straight channels, a thermal boundary layer develops along the flow direction, leading to a gradual increase in the coolant's temperature [24,25]. To mitigate this effect, the introduction of metal foams or obstacles can promote the redevelopment of the thermal boundary layer. The crossflow mixing induced by metal foam within the channels disrupts boundary layer formation, effectively reducing the undesirable temperature rise of the coolant along its path. This approach enhances heat transfer and improves cooling efficiency [24,25]. Additionally, incorporating metal foam enables the cooling system to achieve desired temperatures at lower flow rates, further optimising energy use. However, the accompanying increase in pressure drop due to metal foam must be carefully managed to ensure system efficiency and reliability [25,26]. Du et al. [27] conducted a numerical study on a BTMS for 18,650 LIBs using liquid-cooling channels filled with triply periodic minimal surface (TPMS) porous structures. They demonstrated that incorporating primitive TPMS structures reduced the maximum battery temperature by 12.43 % and improved thermal uniformity by 8.41 % compared to conventional straight tube cooling. Additionally, increasing the porous structure volume fraction to 20 % provided the best balance between heat dissipation and pressure drop. Rabiei et al. [28] carried out a numerical study on a HBTMS based on water and aluminium foam for $LiFePO_4$ prismatic batteries. They demonstrated that the implementation of wavy microchannels significantly reduced pumping power requirements between 50 % to 73 %. Similarly, incorporating a thin metal foam layer decreased pumping power by 50 %. Ki et al. [25] conducted a combined experimental and numerical study on BTMS based on liquid cooling and aluminium foam layer for pouch-type LIBs. Their proposed BTMS achieved 43.3 °C as the maximum cell temperature and maintained a temperature difference of below 2 °C with a flow rate of only 3 L/min. This system leveraged the aluminium foam layer to increase the heat transfer area and reduce thermal dispersion resistance. Jiang et al. [29] numerically analysed a HBTMS for prismatic LIBs integrating active cooling through water-filled mini-channels and passive cooling with a PCM heat sink enhanced by porous media. The obtained results indicated a reduction in maximum temperatures by 13 K at a 3C discharge rate while maintaining energy efficiency with only a 14 % increase in pumping power. Jongpluempiti et al. [30] conducted an experimental and numerical investigation on a liquid-cooled HBTMS for a module composed of 18,650 LIBs. The study evaluated two cooling configurations, one incorporating copper foam and one without, under a constant 0.13C discharge rate. The results indicated that the inclusion of copper foam enhanced heat transfer by increasing the surface area and promoting coolant mixing. This led to a reduction in maximum battery temperature from 27.4 °C to 26.3 °C and improved temperature uniformity, decreasing the maximum temperature difference from 0.75 °C to 0.35 °C. Ningegowda et al. [31] performed a numerical investigation of immersion cooling for 18,650 LIBs using splitter hole configurations. The study compared hole diameters of 2 mm and 3 mm, demonstrating that the smaller diameter facilitated improved cooling performance due to increased flow velocity. Among the tested configurations, Case-3, which featured a reduction in splitter holes along the row-wise direction, achieved the most uniform temperature distribution.

Combining active and passive cooling as hybrid battery thermal management system (HBTMS) has emerged as a promising thermal management method [32,33]. The integration of metal foam significantly enhances both active and passive heat transfer, owing to its interconnected pore structure, which facilitates multiple modes of heat transfer [15]. More importantly due to the structure of the metal foams the overall mass of the HBTMS could considerably be reduced, thereby contributing to higher energy density [34]. Khaboshan et al. [35] implemented a numerical study on a HBTMS for 18,650 LIBs incorporating PCM, copper foam, and fins. This configuration achieved a surface temperature reduction of 3 K by enabling effective heat distribution through the system's core. Similarly, Liu et al. [36] numerically investigated water-based HBTMS with PCM28HC, PCM35HC, and copper foam. Their study demonstrated that helical cooling channels outperformed straight channels, reducing the maximum temperature by over 30 K compared to natural convection. Zhao et al. [37] numerically showed that adding copper foam to a PCM module reduced the surface temperature of 18,650 batteries by 14 °C, maintaining system temperature near the PCM melting point during extended operation. Mashayekhi et al. [38] experimentally studied the thermal phases in an HBTMS for 18,650 batteries, demonstrating that conduction dominated the initial melting phase of the PCM, while convection became the primary mode of heat transfer in the middle stages. Their findings emphasised the importance of optimising materials and configurations to maintain temperature uniformity and safety. Yang et al. [39] proposed a novel HBTMS for 40 Ah prismatic LIBs, integrating TPMS structures, PCM, and liquid cooling, along with a delayed cooling strategy based on battery temperature thresholds. Their simulations showed that the IWP-type TPMS composite enhanced PCM thermal conductivity to 21.3 W/(m·K) and increased the melting rate by 2.7 times compared to rectangular cavities. The delayed cooling scheme raised the PCM liquid fraction from 0.25 to 0.97 while reducing pump energy consumption by 73 %, without compromising temperature safety. Under cyclic conditions, the system demonstrated stable thermal behaviour and efficient latent heat recovery.

While numerous studies have explored the use of metal foams in BTMSs to enhance the thermal conductivity of PCMs or to improve liquid cooling efficiency, there remains a significant gap in the literature concerning their simultaneous and optimised integration in HBTMSs that combine both active and passive cooling strategies. Most existing research has focused on traditional solid fin configurations, overlooking the enhanced thermal performance offered by advanced structures such as metal foam fins. Metal foam, due to its high porosity and large surface area, can improve conduction within the PCM for passive cooling and simultaneously enhance forced convection in liquid cooling channels, thus delivering a dual-mode thermal advantage. The majority of prior work has concentrated solely on thermal behaviour, without addressing the potential to improve system energy density. This is an important factor that is influenced by the structural characteristics and integration of metal foam. Therefore, a comprehensive design strategy that considers both thermal performance and energy density remains underdeveloped.

In the previous study [40], a novel HBTMS integrating PCM, metal foam fins, and liquid cooling with metal foam layers was analysed. The research focused on optimising the porosity and pore density of metal foam to enhance thermal conduction, convective cooling, and energy density. A detailed comparison between metal foam fins and conventional solid fins demonstrated that metal foam fins significantly outperformed solid fins in heat transfer performance, while also providing a 25 % improvement in energy density. The study identified metal foam with a porosity of 0.9 and a pore density of 30 PPI as the optimal configuration for achieving enhanced thermal management and high energy density. While this study established the thermal benefits of metal foam, further investigation is required to broaden its applicability by considering key design parameters, including the influence of structural configurations and external conditions on system efficiency and energy density. Present investigation aims to bridges these gaps by investigating the optimal thickness of metal foam layers, the influence of the number of cooling plates with or without metal foam layers on both thermal performance and energy density, and the impact of ambient temperature on the effectiveness of the system across different operating conditions. By addressing these design parameters, this research provides a more comprehensive framework for integrating metal foam-based HBTMS in practical applications.

2. Defining the problem and introducing the developed HBTMS

The developed HBTMS integrated PCM, liquid cooling, and metal foam, which was utilised both as fins and layers. As depicted in Fig. 1, the pack comprises twelve 18,650 LIBs. Metal foam served dual purposes: as longitudinal fins surrounding the batteries within the PCM and as layers inside the copper tubes. Fig. 1 (a) illustrates the system's various components. To ensure better heat dissipation and prevent direct contact between the PCM and the batteries, each cell was encased in an aluminium housing. To enhance the PCM's thermal conductivity, metal foam fins were embedded longitudinally, and the PCM occupied fins' pores. To regulate the paraffin's phase change, cooling plates made of aluminium with embedded copper tubes were integrated, enabling water to act as the system's coolant. Fig. 1 (b) outlines the engineering drawing of the system with detailed dimensions for different number of cooling plates, which were determined based on standard practices in the literature, manufacturing constraints of metal foam, and standard dimensions for copper tubes.

For this study, 18,650 LIBs (LiNixCoyMnzO2), commonly known as NCM, were utilised due to their high energy density. These batteries are also widely used in electric vehicles [41,42]. The NCM 18650 battery features a nominal voltage of 3.7 V, a nominal capacity of 2.6 Ah, and a mass of 0.0475 kg. Its thermal properties include a radial thermal conductivity of 0.2 $W{\cdot}m^{-1}{\cdot}K^{-1}$, an axial thermal conductivity of 37.6 $W{\cdot}m^{-1}{\cdot}K^{-1}$, and a specific heat capacity of 1200 $J{\cdot}kg^{-1}{\cdot}K^{-1}$ [43]. Aluminium alloy was used for the cooling plates and battery housings, copper foam served as fins and layers, and paraffin was utilised as the PCM. These materials were selected based on their ability to optimise

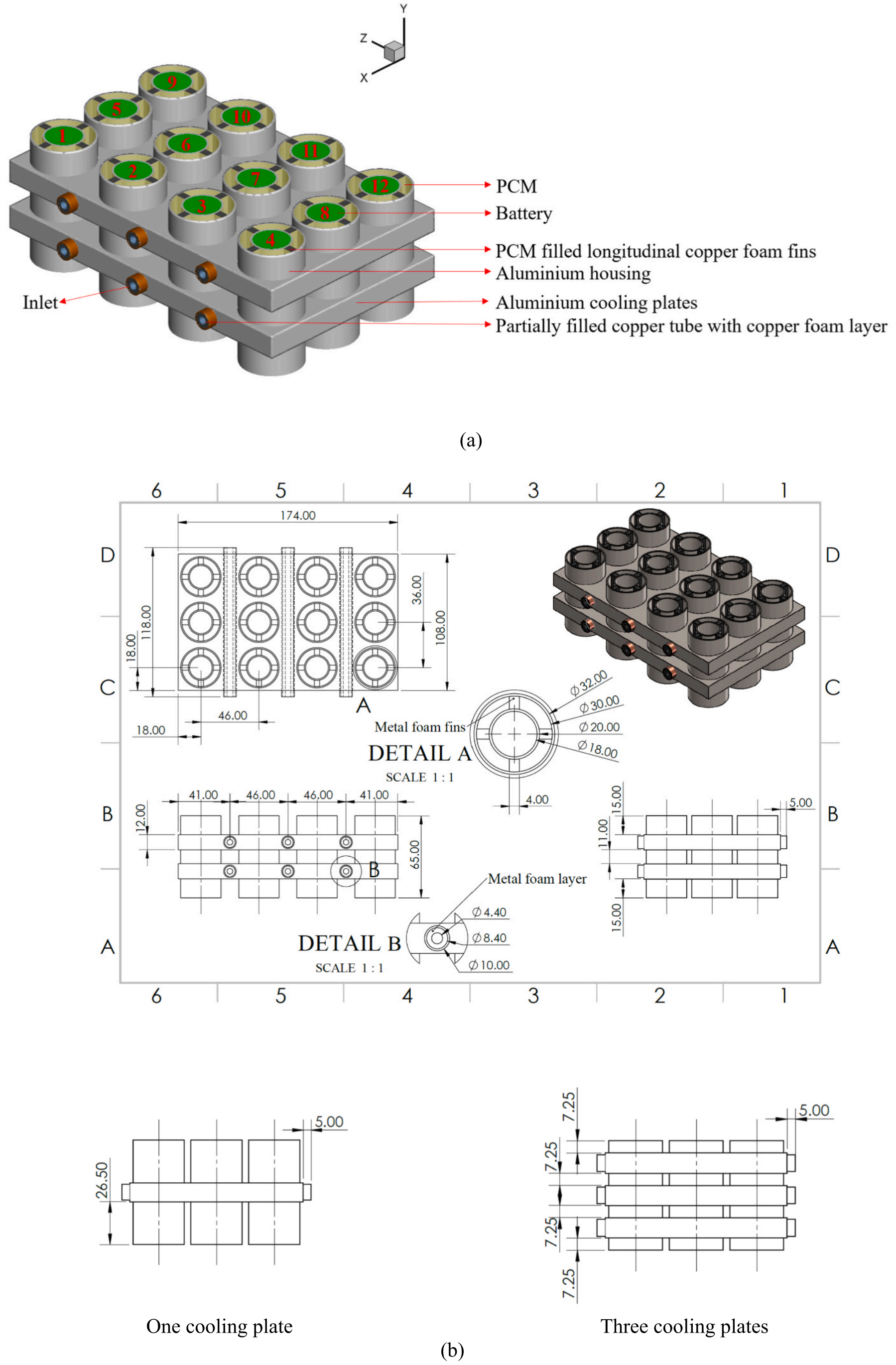

Fig. 1. Proposed HBTMS (a) system components and (b) dimensional specifications for different number of cooling plates.

heat transfer and maintain a lightweight system design, ensuring efficient thermal management and high energy density. The thermophysical properties of the materials were considered based on [40].

3. Numerical modelling

To evaluate the influence of various parameters, including the number of cooling plates (one, two, and three with and without metal foam layer), the thickness of the metal foam layer within the copper tubes (0, 2, 4, 5, 6, and 8.4 mm), and ambient temperature (303.15, 308.15, 313.15, and 318.15 K), on the effectiveness of the proposed HBTMS, 3D simulations were carried out using the commercial CFD software ANSYS FLUENT 23/R2.

3.1. Battery transient heat generation modelling

The lumped-capacitance model was employed to simulate the real-time transient heat generation of the LIBs. This model was found to be appropriate as the calculated Biot number [40] is below 0.1 [44]. This model determines heat generation based on voltage and current characteristics assuming constant thermo-physical properties for the battery [45].

The total generated heat in LIBs based on the Bernardi equation is as follows [43]:

$$Q_t = R_t I^2 - I\left[T\left(\frac{dE}{dT}\right)\right] \tag{1}$$

where Q_t is the total heat generation, I is the electric current, T is the temperature, R_t is the total internal resistance, and $\frac{dE}{dT}$ is the entropy coefficient. The total internal resistance and entropy coefficient are calculated as presented in Table 1 and equation (2), respectively, based on experimental hybrid pulse power characterization (HPPC) test data [46] to model transient battery heat generation for the high discharge rate of 5C. As the discharge rate is the ratio of discharge current to the battery's nominal capacity [47], the corresponding discharge times for 5C is 720 s.

$$\frac{dE}{dT} = -355 \times SOC + 1898 \times SOC^2 - 5121 \times SOC^3 \tag{2}$$

where SOC is the state of charge of the battery.

The heat generation per unit volume of the battery (q_b) is expressed by:

$$q_b = \frac{Q_t}{Vol._{battery}} \tag{3}$$

where $Vol._{battery}$ is the battery volume.

3.2. Governing equations and initial and boundary conditions

To simulate the behaviour of the PCM, enthalpy-porosity model was applied, where the mushy zone, characterized by the coexistence of solid and liquid phases, is considered a porous medium. This model incorporates the effects of latent heat into the energy equation without explicit phase interface tracking [48]. During the melting and solidification processes of a pure PCM without copper foam, three zones are identified: solid, liquid, and mushy. The mushy zone represents a transitional phase where both solid and liquid PCM coexist. In this region, the unmelted PCM forms a solid framework, while the melted PCM fills the gaps, effectively behaving as a porous medium. For composite PCM integrated with metal foam, the liquid phase was also modelled as a porous medium but with a porosity that differs from that of the mushy zone [49].

The representative elementary volume (r.e.v) method was employed for copper foam modelling in conjunction with the Darcy-Brinkman-Forchheimer (DBF) model. The local thermal equilibrium (LTE) model was applied to the metal foam fins, while the local thermal non-equilibrium (LTNE) model was utilised for the metal foam layers within the copper tubes.

Based on the stated assumptions outlined in [40], the governing equations for the PCM and metal foam fins and liquid cooling with metal foam layer are presented in Table 2 and Table 3, respectively.

In Table 2, for the equations applicable to areas without metal foam fins or PCM-only regions, the porosity is set to 1. The momentum equation excludes the source terms since metal foam is not present. Furthermore, L_f is expressed as [55]:

$$L_f = \frac{\Delta H}{h_f} = \begin{cases} 0 \, if T < T_s \\ \dfrac{T - T_{Solidus}}{T_{Liquidus} - T_{Solidus}} T_s \leq T \leq T_l \\ 1 \, if T > T_l \end{cases} \tag{4}$$

where ΔH is latent heat.

Table 1
Total internal resistance in various temperatures [46].

Total internal resistance ($\boldsymbol{R_t}$)	Temperature (K)
$166 - 1334 \times \boldsymbol{SOC} + 6559 \times \boldsymbol{SOC}^2 - 16531 \times \boldsymbol{SOC}^3 + 22391 \times \boldsymbol{SOC}^4 - 15496 \times \boldsymbol{SOC}^5 + 4301 \times \boldsymbol{SOC}^6$	293
$107 - 793 \times \boldsymbol{SOC} + 4036 \times \boldsymbol{SOC}^2 - 10514 \times \boldsymbol{SOC}^3 + 14700 \times \boldsymbol{SOC}^4 - 10480 \times \boldsymbol{SOC}^5 + 2989 \times \boldsymbol{SOC}^6$	303
$66 - 382 \times \boldsymbol{SOC} + 1962 \times \boldsymbol{SOC}^2 - 5181 \times \boldsymbol{SOC}^3 + 7378 \times \boldsymbol{SOC}^4 - 5365 \times \boldsymbol{SOC}^5 + 1559 \times \boldsymbol{SOC}^6$	313
$58 - 355 \times \boldsymbol{SOC} + 1898 \times \boldsymbol{SOC}^2 - 5121 \times \boldsymbol{SOC}^3 + 7367 \times \boldsymbol{SOC}^4 - 5374 \times \boldsymbol{SOC}^5 + 1559 \times \boldsymbol{SOC}^6$	323
$48 - 233 \times \boldsymbol{SOC} + 1225 \times \boldsymbol{SOC}^2 - 3263 \times \boldsymbol{SOC}^3 + 4667 \times \boldsymbol{SOC}^4 - 3406 \times \boldsymbol{SOC}^5 + 992 \times \boldsymbol{SOC}^6$	333

The total enthalpy is defined as:

$$H = h + \Delta H \tag{5}$$

where h is the sensible enthalpy and calculated as:

$$h = h_{ref} + \int_{T_{ref}}^{T} C_{p_f} dT \tag{6}$$

where h_{ref} is the sensible enthalpy at the ambient temperature, which is considered as the reference temperature.

Permeability and coefficient of inertia are given as [56]:

$$K = 0.00073(1 - \varepsilon)^{-0.224} {d_f}^{-1.11} {d_p}^{3.11} \tag{7}$$

$$C = 0.0012(1 - \varepsilon)^{-0.132} \left(\frac{d_f}{d_p}\right)^{-1.63} \tag{8}$$

where d_f and d_p are ligament diameter, pore size, respectively and are defined as [57,58]:

$$d_f = 1.18 d_p \sqrt{\frac{1 - \varepsilon}{3\pi}} \tag{9}$$

$$d_p = 0.0224/\omega \tag{10}$$

where ω is the pore density as pores per inch (PPI).

Based on the LTE model, the effective thermal conductivity is considered as follows [59]:

$$k_{eff} = (1 - \varepsilon) k_s + \varepsilon k_f \tag{11}$$

where k is the thermal conductivity.

In Table 3, permeability of the metal foam layer and the geometric parameter are defined as [60]:

$$K = \frac{\varepsilon^3 d_p^2}{150(1 - \varepsilon)^2} \tag{12}$$

$$C_F = \frac{1.75}{\sqrt{150}\varepsilon^{3/2}} \tag{13}$$

Effective thermal conductivity for solid and fluid phase of the metal foam layer are calculated as follows [61–63]:

$$k_{s_{eff}} = (1 - \varepsilon)^{0.763} k_s \tag{14}$$

$$k_{f_{eff}} = \varepsilon k_f + k_{td} \tag{15}$$

where k_{td} is the coefficient of thermal dispersion based on the following [61–63]:

$$k_{td} = 0.025 \rho_f C_p \sqrt{K} \left| \overrightarrow{V} \right| \tag{16}$$

Fluid-to-solid heat transfer coefficient and specific surface area are defined as follows [64,65]:

$$h_{sf} = \left(\frac{k_f}{d_p}\right)^2 \left(1 + 1.1 \left(\frac{C_{p_f} \mu_f}{k_f}\right)^{1/3}\right) \left(\frac{\rho_f \left|\overrightarrow{V}\right| d_p}{\mu_f}\right)^{0.6} \tag{17}$$

$$a_{sf} = \frac{6(1 - \varepsilon)}{d_p} \tag{18}$$

Table 2
Governing equations for the PCM and metal foam fins [50,51].

Equation	Expression	Description
Continuity	$\frac{\partial \rho_f}{\partial t} + \nabla.\rho_f \vec{V} = 0$	ρ: density, $\vec{V}$: velocity vector
Momentum	$\frac{\rho_f}{\varepsilon}\frac{\partial \vec{V}}{\partial t} + \frac{\rho_f}{\varepsilon^2}\left(\vec{V}.\nabla\right)\vec{V} = -\nabla P +$ $\frac{\mu_f}{\varepsilon}\left(\nabla^2\vec{V}\right) - \rho_{f,ref}\beta_f\varepsilon\left(T - T_{ref}\right)\vec{g} - A_m\frac{(1-L_f)^2}{{L_f}^3 + 0.001}\vec{V} - (\frac{\mu_f}{K} + \frac{\rho_f C\left\|\vec{V}\right\|}{\sqrt{K}})\vec{V}$	ε : porosity, P : pressure, μ : dynamic viscosity, β: thermal expansion coefficient, T : temperature, $\vec{g}$: acceleration due to gravity, $A_m = 10^5$ [52]: mushy zone constant, L_f : liquid fraction, K : permeability, C : coefficient of inertia, $\left\|\vec{V}\right\|$: magnitude of the velocity vector
Energy (Based on LTE method)	$\frac{\partial \varepsilon\rho_f C_{p_f} T}{\partial t} + \nabla\left(\rho_f C_{p_f}\vec{V}.T\right) = \nabla(k_{eff}\nabla T) - \frac{\partial \varepsilon\rho_f L_f h_f}{\partial t} + \nabla\left(\rho_f\vec{V}.TL_f h_f\right)$	C_p : specific heat, k_{eff} : effective thermal conductivity, h_f: latent heat of fusion

Table 3
Governing equations for metal foam layer enhanced liquid cooling [53,54].

Equation	Expression	Description
Continuity	$\frac{\partial \rho}{\partial t} + \nabla.\rho\vec{V} = 0$	ρ: density, $\vec{V}$: velocity vector
Momentum	Clear region: $\rho\frac{\partial \vec{V}}{\partial t} + \rho\nabla.\left(\vec{V}\vec{V}\right) = -\nabla P + \mu_f\left(\nabla^2\vec{V}\right)$Metal foam region: $\rho\frac{\partial \vec{V}}{\partial t} + \frac{\rho}{\varepsilon}\nabla.\left(\vec{V}\vec{V}\right) = -\nabla P + \mu_f\left(\nabla^2\vec{V}\right) - \frac{\mu_f\vec{V}}{K} - \rho C_F\sqrt{\frac{1}{K}}\left\|\vec{V}\right\|\vec{V}$	ε : porosity, P : pressure, μ : dynamic viscosity, K : permeability, C_F : geometric parameter, $\left\|\vec{V}\right\|$: magnitude of the velocity vector
Energy (Based on LTNE method)	Clear region: $\frac{\partial(\rho C_p T_f)}{\partial t} + \nabla\cdot\left(\rho C_p\vec{V}T_f\right) = \nabla\cdot(k_f\nabla T_f)$Metal foam region: Solid phase: $\frac{\partial(\rho_s C_p T_s)}{\partial t} = \nabla\cdot\left(k_{s_{eff}}\nabla T_s\right) - h_{sf}a_{sf}\left(T_s - T_f\right)$Fluid phase: $\frac{\partial(\rho_f C_p T_f)}{\partial t} + \nabla\cdot\left(\frac{\rho_f C_p\vec{V}T_f}{\varepsilon}\right) = \nabla\cdot\left(k_{f_{eff}}\nabla T_f\right) + h_{sf}a_{sf}\left(T_s - T_f\right)$	C_p : specific heat, T: temperature, k : thermal conductivity, h_{sf} : fluid-to-solid heat transfer coefficient, a_{sf}: specific surface area

Adiabatic boundary condition was applied to the bottom of the HBTMS. Constant mass flow rate of 0.001 kg/s was set at the inlet, where the temperature was maintained at 303.15 K, to ensure a balance between maintaining effective cooling performance and minimising pumping power requirements. The porosity and pore density of the copper metal foam have been assumed to be constant at 0.9 and 30 PPI [40], respectively, throughout the study. For water flow in the copper tubes with metal foam layers, the Reynolds number in the unobstructed region was calculated as 151.2, remaining considerably lower than the critical limit of 2000 [66]. Additionally, the permeability Reynolds number for the metal foam layer was determined to be 0.123, which is far below the threshold value of 100 [24,67], confirming laminar flow for all simulations. At the outlet, pressure outlet boundary condition was maintained at atmospheric pressure. No-slip boundary condition was enforced on the walls. For the remaining surfaces, Robin boundary condition (third kind) was applied as follows:

$$-k_{wall}\frac{\partial T_{wall}}{\partial n} = h(T_{Wall} - T_{Amb}) \tag{19}$$

where h represents the convection heat transfer coefficient, which was assumed to be 10 W·m^{-2}·K^{-1} [47] corresponding to air natural convection.

At the solid–liquid interface within the metal foam, the following boundary conditions were applied for LTE and LTNE models. In the LTNE model, the negative sign is retained to explicitly account for the directionality of heat flux, whereas in the LTE formulation, it is typically omitted due to the assumption of temperature continuity across the interface.

LTE [68–70]

$$\vec{V}\Big|_{fluid} = \vec{V}\Big|_{metalfoam} \tag{20}$$

$$\mu_f\frac{\partial \vec{V}}{\partial n}\Bigg|_{fluid} = \mu_{eff}\frac{\partial \vec{V}}{\partial n}\Bigg|_{metalfoam}$$

$$T_{fluid} = T_{metalfoam}$$

$$k_f\frac{\partial T}{\partial n}\Bigg|_{fluid} = k_{eff}\frac{\partial T}{\partial n}\Bigg|_{metalfoam}$$

LTNE [71]

$$\vec{V}\Big|_{fluid} = \vec{V}\Big|_{metalfoam}$$

$$\mu_f\frac{\partial \vec{V}}{\partial n}\Bigg|_{fluid} = \mu_{eff}\frac{\partial \vec{V}}{\partial n}\Bigg|_{metalfoam}$$

$$-k_f\frac{\partial T}{\partial n}\Bigg|_{fluid} = -k_{s_{eff}}\frac{\partial T}{\partial n}\Bigg|_{metalfoam} = q_{interface} \tag{21}$$

$$-k_f\frac{\partial T}{\partial n}\Bigg|_{fluid} = -k_{f_{eff}}\frac{\partial T}{\partial n}\Bigg|_{metalfoam} = q_{interface}$$

The governing equations were solved numerically using the specified boundary and initial conditions. Pressure–velocity coupling was achieved using the SIMPLE scheme. The convective terms were discretised using a second-order upwind scheme, the transient terms were discretised using a second-order implicit time integration scheme, and the diffusion terms were treated through spatial gradient reconstruction using the least squares cell-based method. Convergence criteria were set with residuals of 10^{-4} for the continuity and momentum equations, and 10^{-6} for the energy equation.

3.3. Mesh and time-step independence analysis

The assessment of grid independence was conducted using the Grid Convergence Index (GCI) [72,73], which is defined as:

$$GCI = F_s\frac{|\varepsilon_r|}{r_i^p - 1} \tag{22}$$

where F_s is a safety coefficient and considered to be 1.25 as three grids was compared. p is the convergence rate with theoretical value of 1.97 for a second-order method. The relative error ε_r is calculated as:

$$\varepsilon_r = \frac{f_{i+1} - f_i}{f_i} \tag{23}$$

where f_{i+1} and f_i represent the solution values obtained from the fine and coarse grids, respectively. These values correspond to the maximum temperature of the battery surface at 720 s. The ratio of grid refinement r_i is calculated as:

$$r_{i,i+1} = \frac{h_i}{h_{i+1}} \tag{24}$$

$$h_i = \sqrt[3]{\frac{\sum_{i-1}^{N} \Delta V_i}{N}} \tag{25}$$

where h_i is the average grid spacing, V_i is the volume of each computational cell, and N refers for the total number of grids.

Table 4 presents three different grid densities along with their associated GCI evaluations. For the grid with 6,612,690 computational cells, the GCI is below 3 %, satisfying the grid convergence index criterion [74]. Additionally, the developed mesh is illustrated in Fig. 2.

Various time steps were analysed to ensure time step independence. Table 5 presents the maximum battery surface temperature at 720 s for different time steps. Based on the results, time step of 1 s was deemed suitable for this investigation.

3.4. Validation

The numerical approaches utilised in this investigation were validated through comparison with multiple experimental studies. To verify the lumped-capacitance model, the battery surface temperature was assessed in comparison with experimental data from [46], as shown in Fig. 3 (a). For the validation of the numerical method used to model longitudinal metal foam fins in PCM, the experimental study conducted by Hu et al. [75] was referenced, which incorporated aluminium foam saturated with paraffin. The experimental temperature data were analysed in comparison with the numerical results obtained from both LTE and LTNE methods, as illustrated in Fig. 3 (b). Although both models effectively predicted the temperature of the composite PCM, the LTNE model exhibited a slightly enhanced level of accuracy. However, due to the comparable accuracy of both models and the reduced computational expense of the LTE model, the LTE method was selected for implementation in the simulations of metal foam fins. To verify the integration of metal foam layers within copper tubes, the experimental study conducted by Amani et al. [76] was replicated through simulation. This investigation focused on the water flow through a copper tube embedded with copper foam. The computed values for the average Nusselt number on the tube surface and the associated pressure drop were assessed in comparison with experimental findings, as shown in Fig. 3 (c) and Fig. 3 (d), respectively. As depicted in Fig. 3 (c), the LTNE model demonstrated greater accuracy compared to the LTE model. Consequently, the LTNE model was selected for simulating the metal foam layers within the copper tube. The numerical simulation results across various scenarios exhibited a strong agreement with the experimental data, validating the accuracy and reliability of the numerical models.

4. Results and discussion

4.1. Number of the cooling plate

In this section, the impact of the number of cooling plates in the proposed HBTMS, along with the effect of incorporating metal foam layers at a constant thickness of 4 mm and ambient temperature of 308.15 K, has been investigated.

The impact of the different number of cooling plates with or without metal foam layers on batteries maximum surface temperature ($T_{Max,\ Surface}$) is depicted in Fig. 4 (a) and compared to basic pure PCM BTMS. As shown, for the pure PCM system, the $T_{Max,\ Surface}$ tends to increase rapidly during the 5C discharge reaching approximately 322 K at 720 s. Three distinct stages can be observed, corresponding to the phase change process of the PCM, during which the HBTMS experiences temperature increases with varying slopes. These phases illustrate the thermal storage process within the PCM, encompassing initial sensible heat accumulation before phase transition, latent heat absorption throughout the melting process, and subsequent sensible heat retention following the commencement of melting. The observed temperature increase is attributed to the low thermal conductivity of the pure PCM which results in the accumulation of heat near the battery surfaces and the formation of a melted PCM layer around the battery housing (as shown in Fig. 5 (a)). This layer acts as an insulation around the batteries due to its low thermal conductivity. To mitigate the rapid temperature increase, the implementation of the HBTMS, which incorporates PCM with longitudinal metal foam fins and cooling plates with copper tubes, with or without metal foam layers, led to a significant reduction in $T_{Max,\ Surface}$. So that, as depicted in Fig. 4 (a), employing the HBTMS came up with 8.46, 9.19, and 9.68 K reduction in $T_{Max,\ Surface}$ for HBTMS with one, two, and three cooling plates incorporating metal foam layers, respectively. This reduction is attributed to two key mechanisms introduced by the integration of metal foam. First, the longitudinal copper foam fins embedded in the PCM enhance thermal conduction by acting as highly conductive pathways, which accelerate heat transfer from the battery housing to the outer PCM housing. The metal foam structure increases the effective contact area between the solid foam matrix and the PCM, enabling more uniform and efficient heat transfer. Second, the metal foam layers inside the copper tubes improve forced convection by increasing the internal surface area, disrupting the thermal boundary layer, and promoting enhanced fluid mixing within the coolant flow. These combined effects lead to a substantial improvement in the overall heat transfer capability of the HBTMS. Furthermore, a comparison of cases with varying numbers of cooling plates, with and without metal foam layers, revealed that the inclusion of the metal foam layers resulted in reductions of 2.76 %, 3.24 %, and 3.43 % in $T_{Max,\ Surface}$ for HBTMS configurations with one, two, and three cooling plates, respectively, compared to their counterparts without the metal foam layers. Moreover, a comparison between the configuration of two cooling plates with metal foam layers and the configuration of three cooling plates without metal foam layers revealed $T_{Max,\ Surface}$ values of 312.58 K and 312.41 K, respectively, at 720 s. These results demonstrate that incorporating metal foam layers can effectively reduce the number of cooling plates required in the system while maintaining comparable $T_{Max,\ Surface}$ values.

The number of cooling plates significantly affects the location and extent of PCM melting in the HBTMS, as well as the PCM liquid fraction (L_f), due to enhanced convection within the cooling plates. As shown in Fig. 4 (b), incorporating additional cooling plates with metal foam layers significantly reduced the amount of molten PCM in the HBTMS by 66.06 %, 93.91 %, and 97.51 % for configurations with one, two, and three cooling plates, respectively, compared to the pure PCM system. Additionally, the inclusion of metal foam layers within the copper tubes led to a reduction in the L_f, which is most pronounced in the HBTMS with a single cooling plate. L_f decreased by 32.36 %, 9.01 %, and 6.83 % for HBTMS configurations with one, two, and three cooling plates, respectively, compared to their counterparts without the metal foam layers. Also, the onset of PCM melting as shown in Fig. 4 (b) is significantly delayed by employing HBTMS with cooling plates compared to pure PCM. For instance, for three cooling plates with metal foam layers, the PCM begins to melt at 618 s of the discharge, whereas in the pure PCM system, the onset of melting occurs at 113 s. PCM L_f contour plots at 720

Table 4
Grid Convergence Index (GCI) analysis for various grid densities.

N	h_i	r_i	(f_i) $T_{sur,\ max}$ (K)	ε_r	GCI (%)
4,944,155	1	1.25	313.894287	0.052741	18.30
6,612,690	0.8	1.25	313.897891	0.003603	1.25
11,642,045	0.64	–	313.845152	–	–

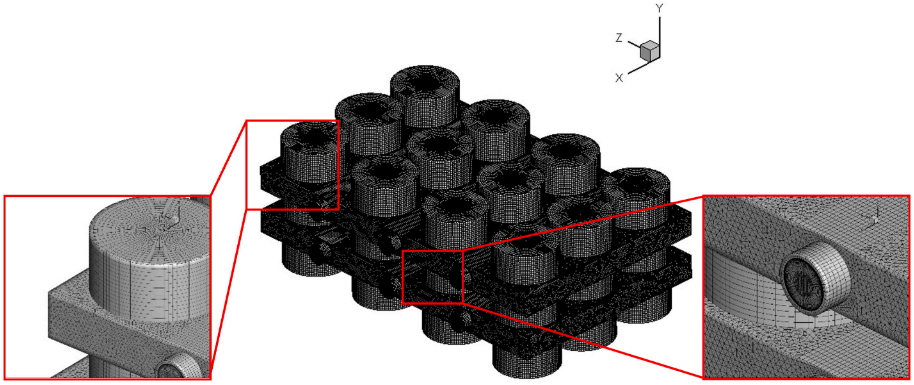

Fig. 2. Mesh configuration for the HBTMS.

Table 5
Evaluation of different time steps.

Time step	$T_{Sur,\ Max}$ (K)	Error (%)
0.25 s	313.9788	–
0.5 s	313.9391	0.012635
1 s	313.8943	0.014271
2 s	313.7315	0.051876

s are provided in Fig. 5. As can be seen, in contrast to pure PCM with extensive melting, particularly around the battery housing, for the HBTMS more confined and localised melting could be observed, predominantly within the metal foam fins. This effect is attributed to the metal foam fins, which enhance the thermal conductivity of the PCM, leading to increased PCM melting within the fins' pores. Moreover, as additional cooling plates, particularly those with metal foam layers, are incorporated into the HBTMS, the amount of melted PCM decreases significantly. In the case of a single cooling plate without metal foam layers (as shown in Fig. 5 (c)), PCM melting is not confined to the fins, and melted PCM can also be observed around the battery and PCM housing. However, as depicted in Fig. 5 (b), (d), and (f), with the inclusion of metal foam layers, the heat conducted through the battery housing and into the PCM, fins, and PCM housing is more efficiently transferred via force convection within the copper tubes, resulting in a reduction in the amount of melted PCM. Similarly, by increasing the number of cooling plates, with or without metal foam layers, less PCM was melted, and the melting was restricted to the pores of the fins with higher thermal conductivity. Also, as shown in Fig. 5, for different

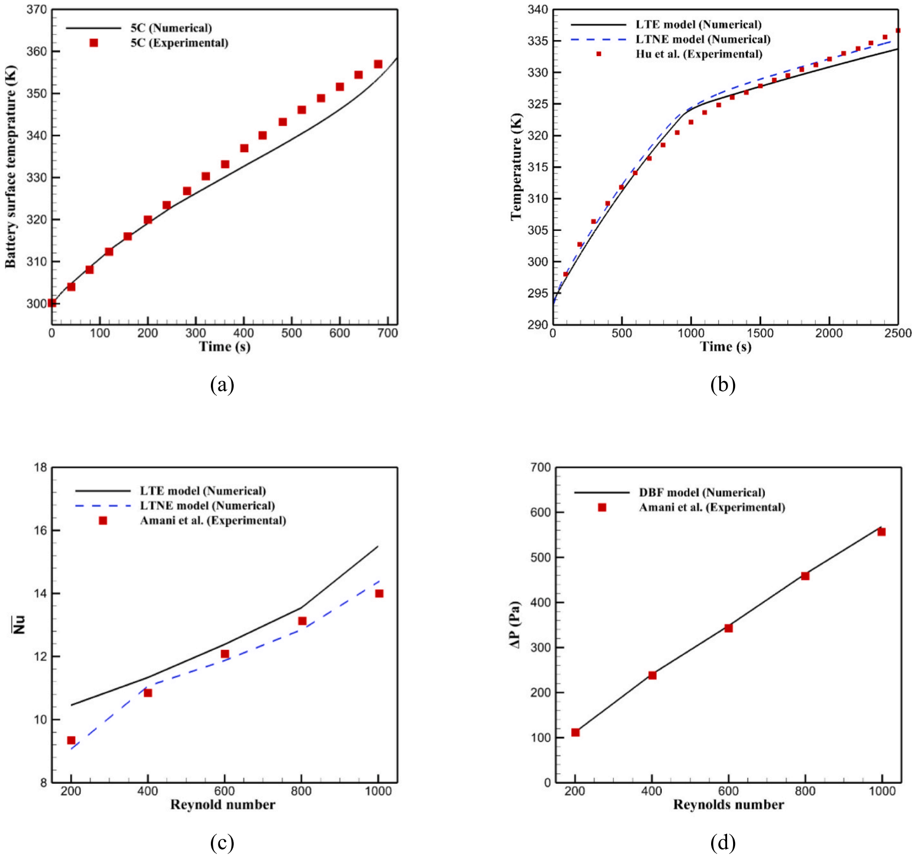

(a) (b)

(c) (d)

Fig. 3. Comparison between (a) the present numerical and experimental surface temperature measurements [46], (b) present numerical and experimental PCM filled metal foam temperatures [75], (c) present numerical and experimental average Nusselt number [76], and (d) present numerical and experimental pressure drop [76].

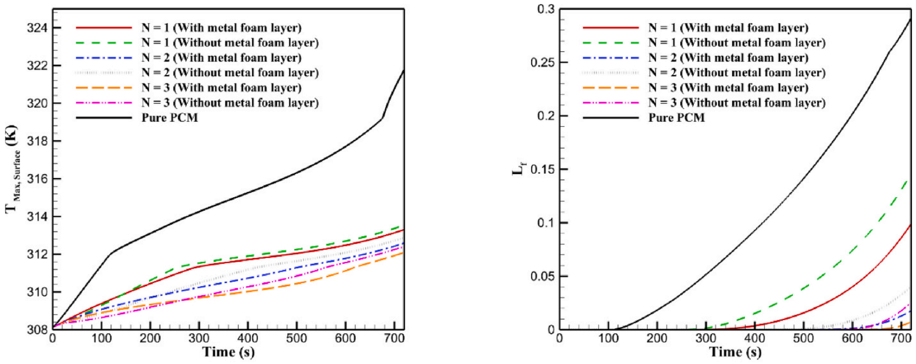

(a)

(b)

Fig. 4. Impact of the different number of cooling plates on (a) batteries maximum surface temperature and (b) PCM liquid fraction.

batteries, less PCM is melted around batteries 1 to 4, particularly batteries 2 and 3, as they are most directly affected by the copper tubes which allows for more efficient local heat extraction. As water flows through the copper tubes toward the outlet, it absorbs increasing amounts of heat, gradually diminishing its capacity for further heat removal. Consequently, more PCM melts around the batteries in the last row, particularly batteries 9 and 12 on the side, with some melted PCM still observed even in the case with three cooling plates.

In order to determine the performance enhancement achieved by the HBTMS, the average Nusselt number on battery surface ($\overline{Nu}_{Battery}$) based on battery surface and PCM melting temperature [77] is illustrated in Fig. 6. For different cases the $\overline{Nu}_{Battery}$ showed a substantial increase up to the point where melting began, and the surface temperature surpassed the PCM solidus temperature. Progressively, it steadily decreased until the discharge process was completed. Compared to pure PCM cooling with limited natural convection cooling, a significant increase in $\overline{Nu}_{battery}$ was observed, with values increasing approximately 7, 13, and 33 times for the HBTMS configurations with one, two, and three cooling plates, respectively. As previously discussed, this improvement is attributed to the addition of longitudinal metal foam fins to the PCM surrounding the batteries and the implementation of liquid cooling via cooling plates, particularly through enhanced force convection within the copper tubes with metal foam layers. The incorporation of fins enhances the thermal conductivity of the pure PCM by establishing conduction pathways that significantly improve heat transfer from the battery housing to the PCM housing. As the PCM melts within the fin pores, natural convection complements conduction, with the pores facilitating fluid movement that enhances heat transfer through internal mixing and circulation. Moreover, the metal foam structure increases the surface area, further improving heat transfer efficiency. Additionally, the insertion of metal foam layers significantly impacts the velocity and temperature profiles within the copper tube, directly influencing force convection efficiency. The dimensionless velocity and temperature profile, based on [78], along the vertical axis at the central section of the copper tube is compared in Fig. 7 for a 4 mm thick metal foam layer and a clear copper tube in the case of two cooling plates. As shown in Fig. 7 (a), the metal foam layer introduces flow resistance, with a steeper velocity gradient at a further distance from the copper tube wall compared to the clear copper tube. This promotes greater mixing near the wall, where the high thermal conductivity of the metal foam enhances heat transfer. At the tube's core, the fluid velocity in the clear region is approximately 1.75 times greater than in a tube without the metal foam layer, further improving convection at the interface of the metal foam layer. The dimensionless temperature profile, as presented in Fig. 7 (b), further supports this observation, illustrating that the temperature distribution becomes discontinuous upon the inclusion of the metal foam layer. Water as the liquid phase within the metal foam exhibits a higher temperature compared to the water temperature in the clear tube, indicating improved heat dissipation from the copper tube facilitated by the expanded surface area offered by the foam's ligaments. Furthermore, the high thermal conductivity of the metal foam and the disruption of the thermal boundary layer by the ligaments further enhance heat transfer efficiency.

Each battery $T_{Max,\ Surface}$ and maximum surface temperature difference ($\Delta T_{Max,\ Surface}$) for the HBTMS and pure PCM is provided in Fig. 8 along with static temperature contour plots in Fig. 9. As shown in Fig. 8 (a), for pure PCM cooling, all the batteries reached a nearly same high $T_{Max,\ Surface}$ of approximately 322 K, with $\Delta T_{Max,\ Surface}$ maintained around 0.65 K. Almost uniform temperature distribution along each battery, which is also evident in Fig. 9 (a), was obtained due to considering aluminium housing around batteries, which facilitates radial heat conduction and promotes a relatively even temperature distribution. Introducing HBTMS, as shown in Fig. 8 (b) reduced the $T_{Max,\ Surface}$ on each battery. As result of cooling plates with liquid cooling the batteries 1, 4, 5, 8, 9, and 12 located on the sides of the pack experienced higher $T_{Max,\ Surface}$ compared to batteries 2, 3, 6, 7, 10, and 11. Also as shown in Fig. 9 (b), the static temperature is lower for batteries close to the liquid cooling inlet and the centre of the pack, whereas the highest core temperatures were observed in cells positioned on the sides and at the last row of the pack. This is attributed to the fact that the middle cells are more effectively cooled by the liquid cooling system with metal foam layers, as they are closer to the copper tubes. In terms of the $\Delta T_{Max,\ Surface}$, in contrast to pure PCM cooling, fluctuations were observed in HBTMS with a maximum around 0.7 K on batteries 1 and 4, which are more affected by liquid cooling from one side. However, this value is significantly below the expected $\Delta T_{Max,\ Surface}$ of 5 K in the literature [9,79]. Similar to pure PCM cooling, as shown in Fig. 9 (b), almost uniform temperature distribution on battery surface was achieved by HBTMS with considerable reduction compared to pure PCM cooling. Therefore, novel implementation of battery housing could provide uniform temperature beside preventing direct contact of the PCM with battery due to safety considerations. This uniformity is essential for battery performance and longevity, as it mitigates thermal stresses among cells and reduces the risk of temperature-driven degradation or imbalance within the battery pack.

Energy density, which is a measure of the amount of energy stored per unit mass of a system [80], is an important factor that requires consideration when designing and developing HBTMS and is calculated as follows [80]:

$$E_d = \frac{UC_0}{m} \tag{26}$$

where E_d refers to the energy density, U is the nominal voltage of the battery, C_0 denotes its nominal capacity, and m represents the total mass of the HBTMS.

An ideal design achieves a balance between high cooling efficiency

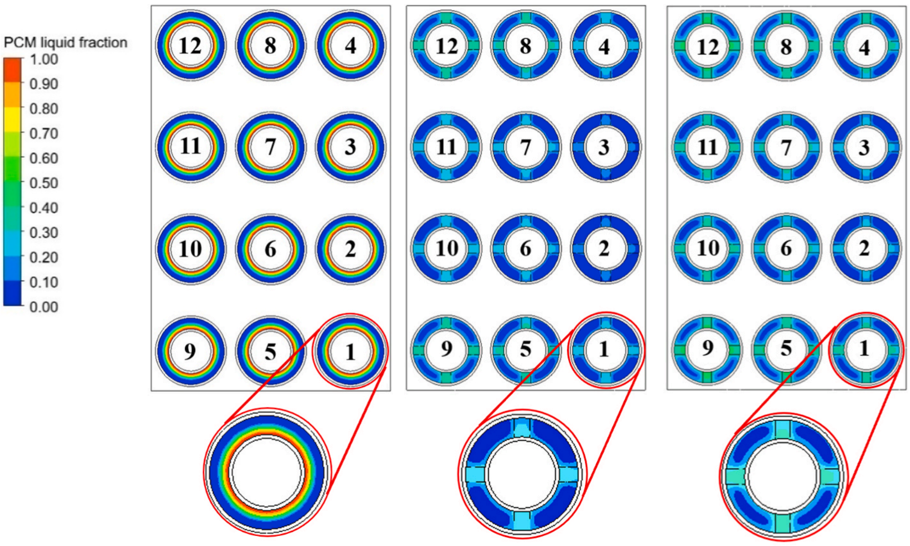

(a) Pure PCM

(b) One cooling plate with metal foam layers

(c) One cooling plate without metal foam layers

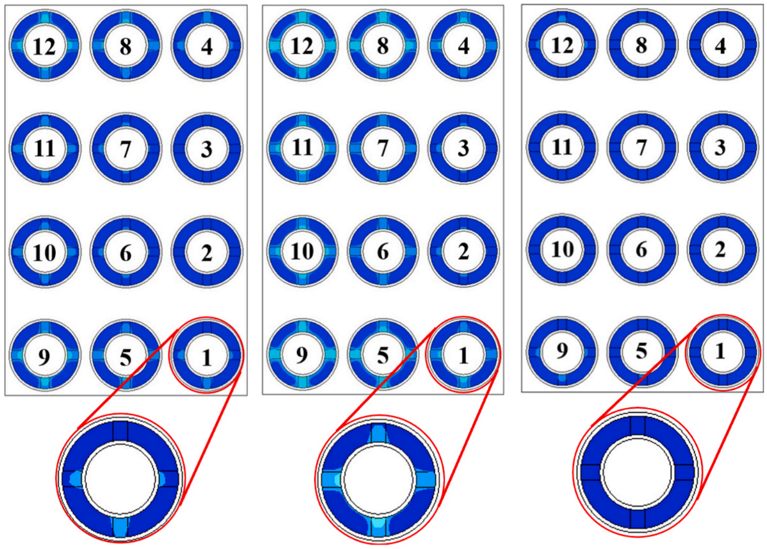

(d) Two cooling plates with metal foam layers

(e) Two cooling plates without metal foam layers

(f) Three cooling plates with metal foam layers

Fig. 5. PCM liquid fraction contour plots for pure PCM cooling and HBTMS with different number of cooling plates at 720 s.

and minimal mass, preserving battery pack energy density while maintaining adequate thermal control. As shown in Fig. 10, the number of cooling plates significantly affects the energy density of the HBTMS due to the additional weight added to the batteries in the pack. Comparing configurations with the same number of cooling plates, with and without metal foam layers, reveals that the inclusion of the metal foam layers slightly reduces the energy density.. The porous nature of the foam adds a relatively low mass, especially when compared to the mass of full cooling plates.. Considering the comparable performance of the HBTMS with three cooling plates without metal foam layers and two cooling plates with metal foam layers in terms of $T_{\text{Max, Surface}}$ (Fig. 4 (a)), $\overline{Nu}_{Battery}$ (Fig. 6), and amount of melted PCM (Fig. 5), the two cooling plates configuration with metal foam layers was preferred, resulting in an 11 % improvement in energy density. This improvement highlights the ability of metal foam to compensate for the reduced surface area resulting from fewer cooling plates, leading to a lighter and more energy-dense design without compromising on thermal safety and operational efficiency.

4.2. Metal foam layer thickness

In this section the impact of different metal foam layer thickness on the performance of the HBTMS with two cooling plates at the ambient temperature of 308.15 K has been investigated.

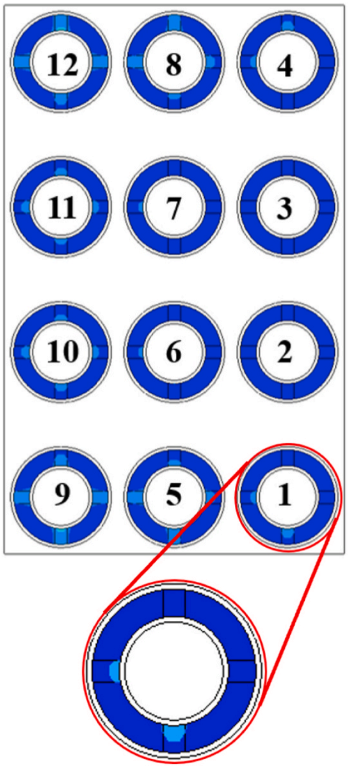

(g) Three cooling plates without metal foam layers

Fig. 5. (*continued*).

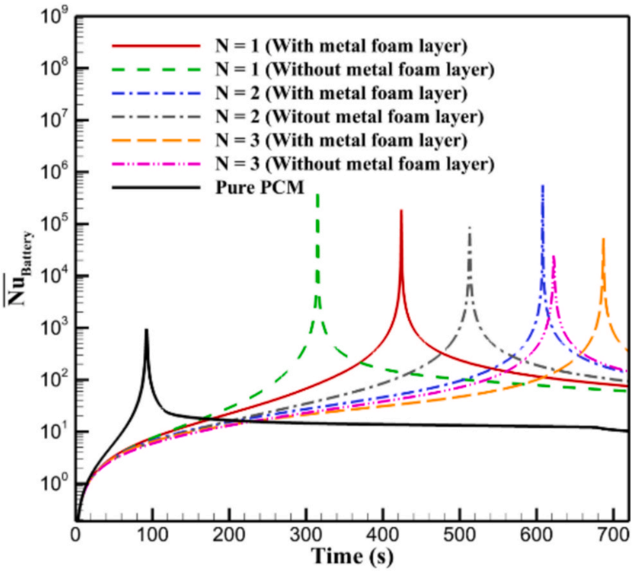

Fig. 6. Battery surface average Nusselt number for pure PCM cooling and HBTMS with different number of cooling plates at 720 s.

The influence of various metal foam layer thickness on $T_{Max,\ Surface}$ is shown in Fig. 11 (a). Compared to copper tube without any metal foam layer, it is evident that $T_{Max,\ Surface}$ was reduced when the copper tube was partially filled. As the thickness increases, the foam's interconnected pores offer additional surface area for heat exchange and disrupt the developing thermal boundary layer, which improves the overall active heat removal from the system. However, when the metal foam layer thickness is 8.4 mm and the tube is completely filled, convection was hindered by the increased flow resistance, making conduction through the foam ligaments the dominant heat transfer mechanism. As result $T_{Max,\ Surface}$ reached 313.69 K at 720 s for thickness of 8.4 mm. Reducing the thickness to 0, 2, 4, 5, and 6 mm resulted in decreases in $T_{Max,\ Surface}$ by 0.8, 0.82, 1.11, 1.25, and 1.45 K, respectively. As force convection heat transfer rate is altered by metal foam layer thickness variation, as shown in Fig. 11 (b), more PCM was melted by fully filled copper tube peaking at $L_f = 0.19$ at 720 s. As the thickness of 0, 2, 4, 5, and 6 mm were considered, L_f was reduced by 79.21 %, 65.44 %, 90.82 %, 89.21 %, and 94.7 %, respectively. Also, the onset of PCM melting was affected when the tube is partially filled and delayed by 159, 178, 262, 304, and 341 s for the thickness of 0, 2, 4, 5, and 6 mm, respectively, compared to the fully filled tube.

Each battery's $T_{Max,\ Surface}$ and $\Delta T_{Max,\ Surface}$ with various metal foam layer thickness is demonstrated in Fig. 12 at 720 s. Partially filled tubes consistently show better overall cooling performance, as indicated by a lower $T_{Max,\ Surface}$ across the pack. The highest $T_{Max,\ Surface}$ was observed on batteries 9 and 12, located on the side of the last row, where the impact of liquid cooling is minimal after absorbing heat upstream. Lowest $\Delta T_{Max,\ Surface}$, as depicted in Fig. 12 (f), was achieved by the fully filled copper tube maintaining values mostly between 0.3 and 0.5 K. This is explained by the dominance of conductive heat transfer through the fully packed foam, which lowers temperature gradients but limits the coolant's convection-driven heat removal. As the thickness was increased from 0 to 6 mm, $\Delta T_{Max,\ Surface}$ was also increased but remained below 1 K. Also, it was observed that increasing the thickness primarily affected $\Delta T_{Max,\ Surface}$ on batteries 1 to 4 in the first row, where the best cooling performance occurred due to their proximity to the inlet section of the cooling plates.

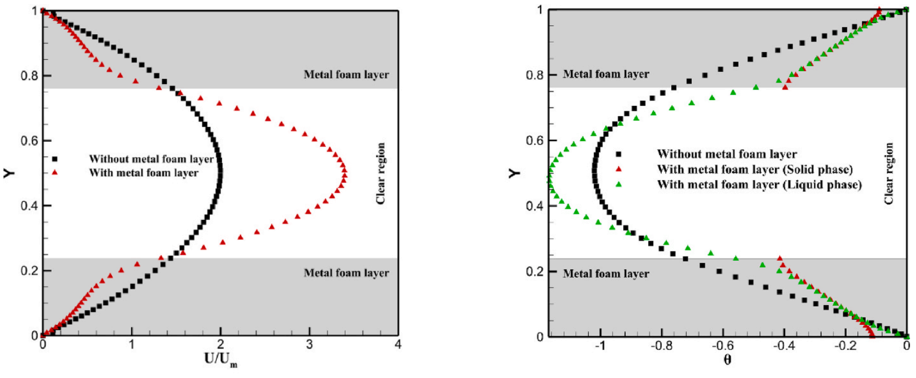

(a) (b)

Fig. 7. (a) Dimensionless velocity and (b) temperature within the copper tube with and without metal foam layer at 720 s.

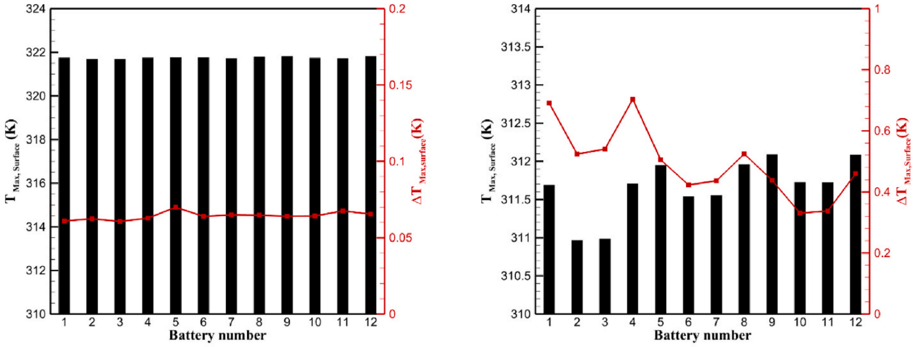

(a) Pure PCM (b) Three cooling plates with metal foam layers

Fig. 8. Comparison of the $T_{Max,\ Surface}$ and $\Delta T_{Max,\ Surface}$ of the pure PCM cooling and HBTMS with three cooling plates with metal foam layers at 720 s.

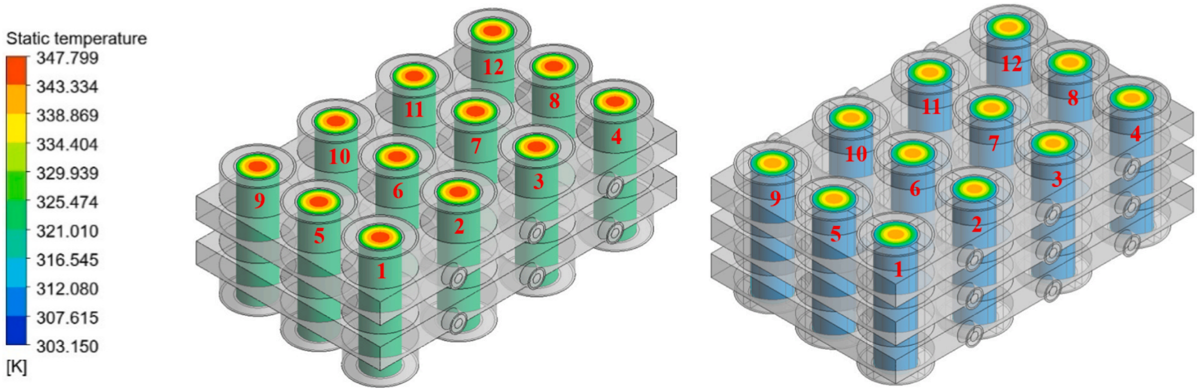

(a) Pure PCM (b) Three cooling plates with metal foam layers

Fig. 9. Comparison of the static temperature contour plots of pure PCM cooling and the HBTMS with three cooling plates with metal foam layers at 720 s.

As shown in Fig. 12 (a) to (f), for different metal foam layer thickness the maximum $T_{Max,\ Surface}$ and $\Delta T_{Max,\ Surface}$ values were recorded on batteries 12 and 4, respectively. To provide a clearer perspective on these results, the corresponding trends are presented in Fig. 12 (g). It can be observed that as the metal foam layer thickness increases, the $T_{Max,\ Surface}$ generally decreases, reaching a minimum value with a 6 mm layer, which corresponds to a 0.611 K reduction compared to the clear copper tube. However, further increasing the thickness to 8.4 mm (fully filled copper tube) leads to a 2.6 % increase in $T_{Max,\ Surface}$, due to reduced convective flow caused by excessive flow resistance. In terms of $\Delta T_{Max,\ Surface}$, a slight initial reduction of 0.05 K is observed with a 2 mm layer. However, as the thickness increases, $\Delta T_{Max,\ Surface}$ rises and peaks at 0.830 K with a 6 mm layer which is approximately a 30 % increase compared to the clear copper tube. Notably, the fully filled copper tube configuration (8.4 mm) results in a 25 % reduction in $\Delta T_{Max,\ Surface}$ compared to the clear copper tube, indicating improved thermal uniformity at the cost of higher overall temperature.

Impact of various metal foam layer thickness on $\overline{Nu}_{Battery}$ is depicted

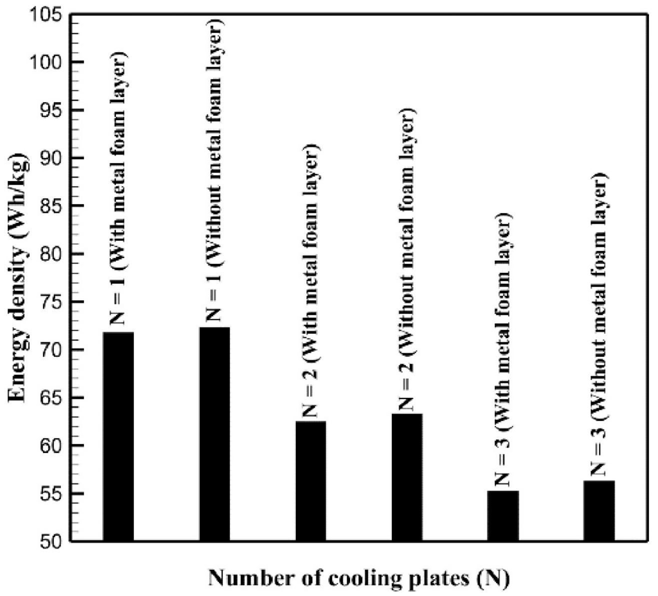

Fig. 10. Energy density of the HBTMS with different number of cooling plates with or without metal foam layers.

in Fig. 13. As shown, $\overline{Nu}_{Battery}$ peaked at different stages of discharge due to the delay in the onset of PCM melting and the battery surface temperature exceeding the PCM solidus temperature. When the tube was fully filled with metal foam, the lowest $\overline{Nu}_{Battery}$ value of 42.7 was recorded at 720 s. By considering partially filled tubes, $\overline{Nu}_{Battery}$ was improved by 2.18, 2.1, 3.16, 4.10 and 6.49 times compared to a fully filled copper tube for metal foam layer thicknesses of 0, 2, 4, 5, and 6 mm, respectively. This enhancement is attributed to the effect of metal foam layer thicknesses on the dimensionless velocity and temperature distribution within the copper tube, as illustrated in Fig. 14. As shown in Fig. 14 (a), the dimensionless fluid velocity within the metal foam layer is lower than in the clear domain, and the uniform velocity distribution observed in a fully filled or clear copper tube is significantly altered by the partially added metal foam layer. This alteration is attributed to the additional flow retardation and mixing caused by the microscopic inertial and viscous forces generated by the solid matrix of the metal foam. As the metal foam creates additional flow resistance near the tube wall, lowering the local velocity within the foam region but redirecting coolant toward the clear domain and increasing its maximum velocity. Consequently, a more pronounced velocity gradient emerges, leading to stronger forced convection along the interface between the foam and the clear region. Also, partial filling reduces the significant pressure drop associated with fully filled tubes. Similarly, as demonstrated in Fig. 14 (b), the uniform dimensionless temperature distribution in a clear tube and the uniform solid and liquid phase temperature distribution in a fully filled tube are influenced by the presence of a partially added metal foam layers. This effect arises from the metal foam's impact on conduction and convection heat transfer within the copper tube. The enhancement in conduction and convection is primarily attributed to the metal foam layer's ability to improve fluid mixing, the increased effective thermal conductivity of the fluid, and the formation of a thinner hydrodynamic boundary layer, which reduces thermal resistance. Additionally, as the thickness increases, the development of the thermal boundary layer becomes more pronounced due to the enhanced velocity and temperature gradients near the interface of the metal foam layer and the walls. Thicker metal foam layers further amplify heat transfer by intensifying velocity gradients, strengthening thermal gradients, and enhancing the interaction between conduction and convection at the interface. Moreover, as illustrated in Fig. 14 (b), increasing the foam thickness enhances the development of a thermal boundary layer near the tube wall. However, beyond a certain point, the benefits of improved conduction are offset by reduced coolant flow, indicating diminishing returns. Therefore, the optimal foam thickness is defined as the one that significantly improves local mixing and heat transfer without causing excessive flow deceleration. As observed, the solid phase temperature is higher for different thicknesses, with the highest value recorded for the 4 mm metal foam layer thickness. This indicates improved conduction in the vicinity of the copper tube's wall. Also, a temperature difference was observed at the interface between the metal foam layer and the clear region of the tube, including between the solid and liquid phases within the metal foam layer and the fluid temperature in the clear region. The increased fluid velocity at the interface, resulting from greater metal foam thickness, enhances force convection at the boundary between the metal foam layer and the clear region. The elevated fluid temperature at the tube's core, particularly for metal foam thicknesses exceeding 2 mm, serves as evidence of improved heat transfer and more effective heat removal from the copper tube wall. However, as shown in Fig. 14 (b), the maximum fluid temperature at the core for a 2 mm thickness is lower than that of the clear tube, resulting in a lower $\overline{Nu}_{Battery}$ as observed in Fig. 13. Also, as depicted in Fig. 14 (a), the dimensionless velocity at the core of the copper tube increases with the thickness of the metal foam layer up to 5 mm, reaching a maximum value of 3.68. However, further increasing the thickness to 6 mm reduces the maximum velocity to 3.37, which is slightly lower than the 4 mm case, where the maximum velocity is 3.39. As the thickness of the metal foam layer increases, occupying a significant cross-sectional area of the copper tube, and given the assumed porosity of 0.9 and pore density of 30 PPI [40], more fluid flow starts to penetrate into the metal foam. This results in a decline in the maximum velocity at the core of the tube. This observation is consistent to the results reported in the literature [81–83]. This phenomenon significantly impacts heat transfer performance, as reflected in the $T_{Max,}$

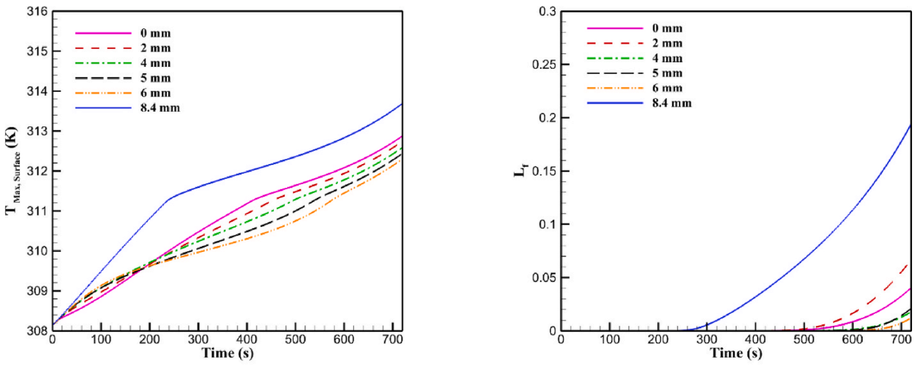

(a)

(b)

Fig. 11. Impact of the metal foam layer thickness on (a) batteries maximum surface temperature and (b) PCM liquid fraction.

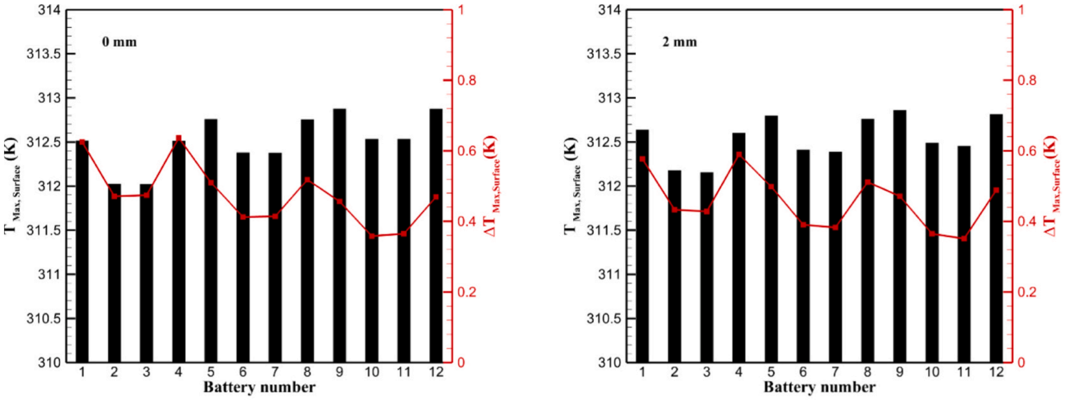

(a) 0 mm

(b) 2 mm

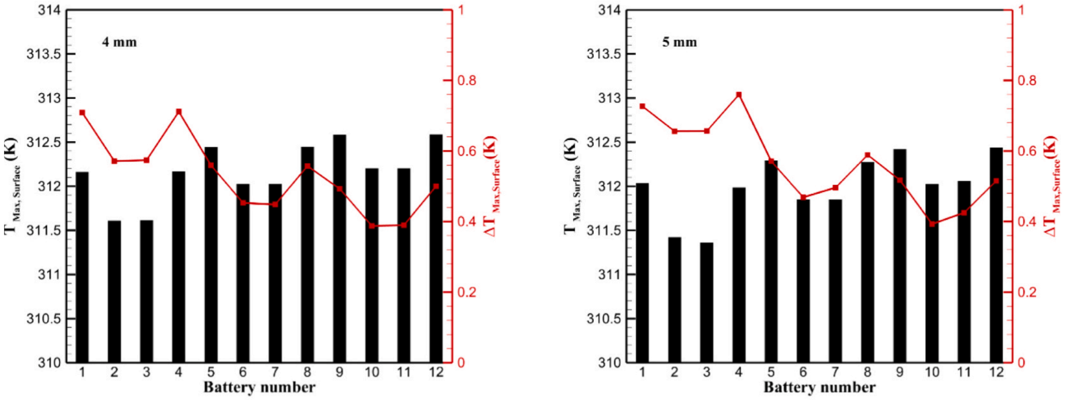

(c) 4 mm

(d) 5 mm

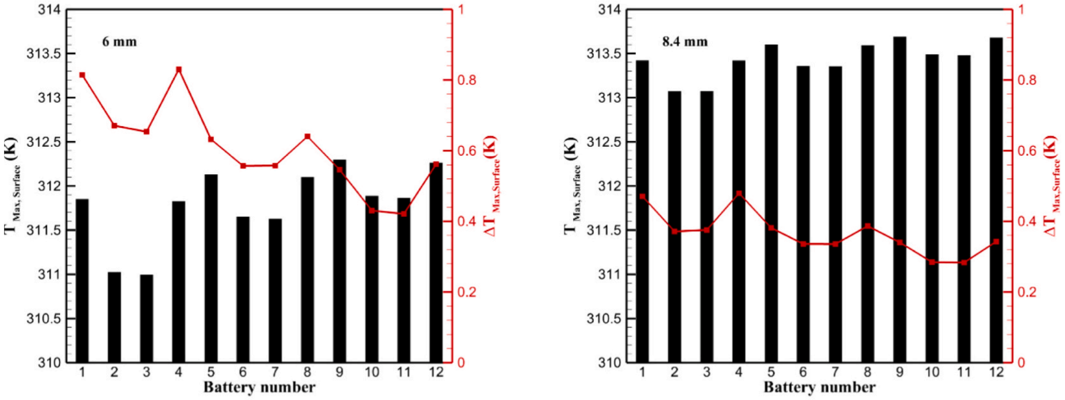

(e) 6 mm

(f) 8.4 mm

Fig. 12. Comparison of the $T_{Max,\ Surface}$ and $\Delta T_{Max,\ Surface}$ of the HBTMS with different metal foam layer thickness at 720 s.

$_{Surface}$ and $\overline{Nu}_{Battery}$.

The pressure drop was observed to increase with the insertion of a thicker metal foam layer in the copper tube. Therefore, it is crucial to maintain a balance between the enhanced heat transfer and the increased pressure drop, which is an unfavourable factor in thermal management systems. The performance evaluation criteria (PEC) [84] which analyses the impact of metal foam layers within the copper tube on the Nusselt number and pressure drop, can be utilised to identify an optimal thickness. The PEC value is calculated as follows [84]:

$$PEC = \frac{\overline{Nu}/\overline{Nu}_0}{\left(\overline{f}_r/\overline{f}_{r0}\right)^{1/3}} \tag{27}$$

where $\overline{Nu}$ and $\overline{f}_r$ represent the average Nusselt number for the liquid cooling and the average friction factor, respectively, and are defined as follows:

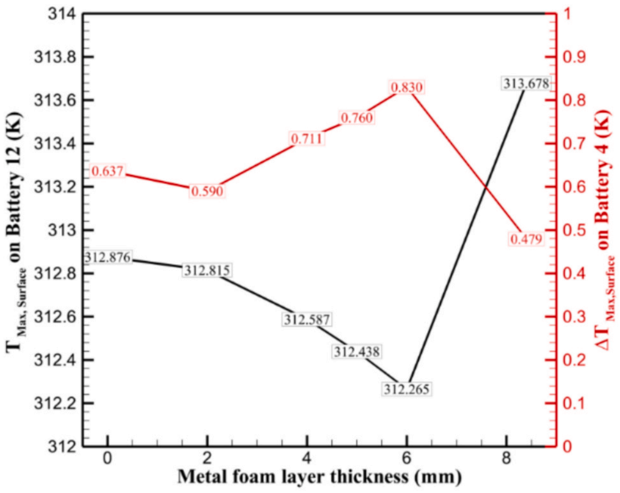

(g)

Fig. 12. (*continued*).

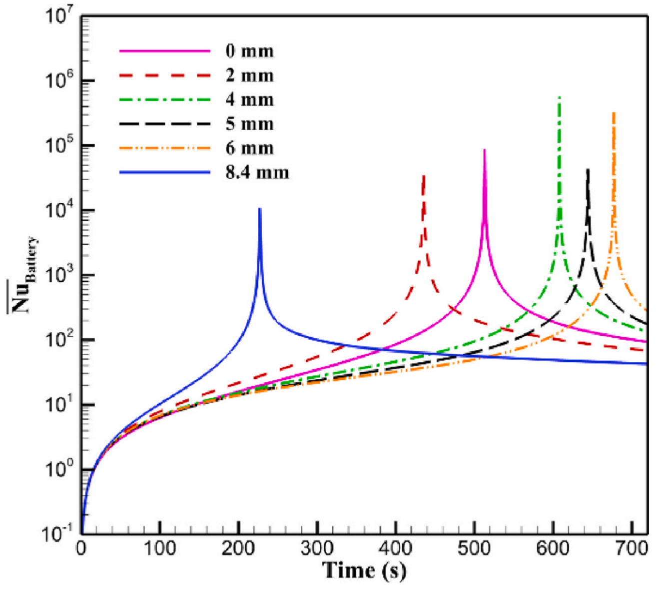

Fig. 13. Batteries surface average Nusselt number for HBTMS with different metal foam layer thickness at 720 s.

$$\overline{Nu} = \frac{\overline{h}D}{K_f} \tag{28}$$

where $\overline{h}$, D, and K_f denote the average convective heat transfer coefficient, the inner diameter of the copper tube, and the thermal conductivity of water, respectively.

$$\overline{f_r} = \frac{\Delta P}{\rho_f U_{inlet}^2} \tag{29}$$

where ΔP, ρ_f, and U_{inlet} correspond to the pressure drop in the copper tube, the density of water, and the inlet flow velocity, respectively.

The PEC values for different metal foam layer thicknesses are provided in Fig. 15. A PEC value below 1 indicates that the increase in pressure drop outweighs the enhancement in heat transfer, as observed for the fully filled copper tube, which has a PEC value of 0.11. For partially filled copper tubes with different thicknesses, the PEC values exceed 1, indicating improved performance compared to the fully filled case. Notably, for a thickness of 4 mm, the PEC value is higher than that of other thicknesses, highlighting 4 mm as the optimal thickness. Increasing the foam thickness beyond this point further develops the thermal boundary layer near the tube wall, which can improve conduction. However, these gains are offset by a sharper reduction in coolant flow, leading to diminished convection especially at the interface of the metal foam layer and clear region. At the 4 mm thickness, the

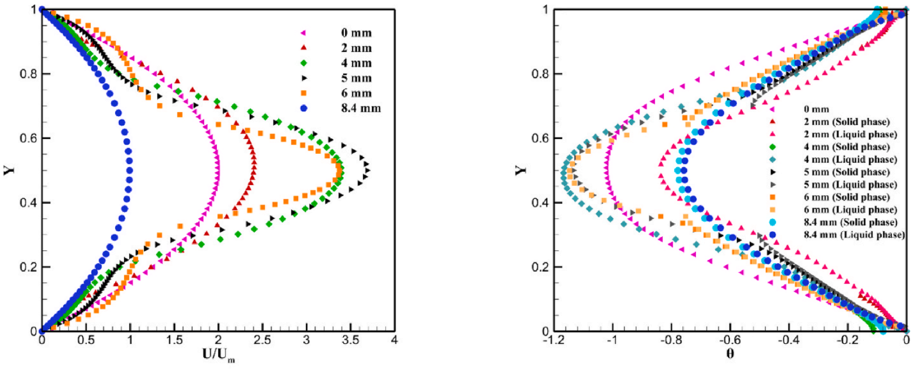

(a) (b)

Fig. 14. (a) Dimensionless velocity and (b) temperature within the copper tube with different metal foam layer thickness at 720 s.

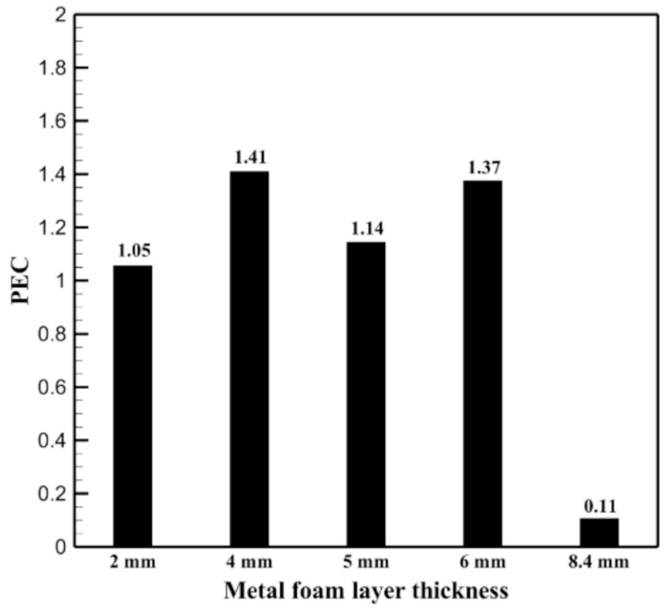

Fig. 15. Impact of metal foam layer thickness on PEC.

foam's ligaments still promote strong local mixing and conduction pathways without causing excessive flow deceleration which results in reduced convective heat transfer and excessive pressure drop. Therefore, the optimal thickness of 4 mm strikes an effective balance between enhanced heat transfer and increased pressure drop, while the porosity of 0.9 contributes to maintaining a high energy density for the system.

4.3. Ambient temperature

In this section, the impact of varying ambient temperatures on the performance of the HBTMS with two cooling plates and 4 mm metal foam insert thickness has been studied.

The impact of ambient temperature, as a critical factor in HBTMSs with PCM, on the performance of the proposed HBTMS in terms of $T_{Max,\ Surface}$ and L_f during high 5C discharge rate is demonstrated in Fig. 16. As shown in Fig. 16 (a), $T_{Max,\ Surface}$ increased more rapidly during discharge at low ambient temperatures. At lower ambient temperatures of 303.15 K and 308.15 K, $T_{Max,\ Surface}$ rose by 8.67 K and 4.44 K, respectively. In contrast, at higher ambient temperatures of 313.15 K and 318.15 K, the variation of $T_{Max,\ Surface}$ during the discharge was significantly lower, recorded at just 1.7 K and 1.5 K, respectively. This is due to the fact that at ambient temperatures below the PCM solidus temperature (311.15 K), as depicted in Fig. 16 (b), PCM was initially in its solid state, and only partial melting occurred during discharge reaching maximum liquid fraction of 0.02 due to the enhanced liquid cooling provided by the cooling plates. In contrast, at higher ambient temperatures, the PCM is partially melted at the onset of discharge, positioning it closer to its latent heat absorption range and thereby enabling more efficient heat absorption from the batteries. This, in conjunction with the cooling plates, allows for improved control over temperature rise during the discharge process. This underscores the importance of employing hybrid cooling systems with PCM, not only to enhance conduction and convection through the application of fins within the PCM but also to incorporate effective mechanisms, such as cooling plates, for extracting heat fromthe PCM housing under higher ambient temperatures. To provide a more detailed view of the PCM melting process, liquid fraction contour plots of the PCM are presented in Fig. 17 at 720 s. As shown, at the low ambient temperature of 303.15 K, the PCM around the batteries remained unmelted, as the temperature was effectively controlled below the solidus temperature. When the ambient temperature increased to 308.15 K, the PCM was observed to melt primarily within the fins, due to enhanced conduction, with the cooling plates having the most noticeable impact on batteries 1 to 4 in the first row. Similarly, at an ambient temperature of 313.15 K, the PCM was largely melted within the fins and around batteries 9 to 12. A uniform PCM melting pattern was observed, except for batteries 2 and 3, which were more affected by the liquid cooling inlet. At the highest ambient temperature of 318.15 K, the PCM surrounding the batteries was completely melted; however, the HBTMS still effectively controlled the temperature rise. Consequently, as shown in Fig. 16 (a), at high ambient temperatures of 313.15 K and 318.15 K, the proposed HBTMS maintained $T_{Max,\ Surface}$ almost constant and close to the ambient temperature. Additionally, as depicted in Fig. 16 (b), the system recovered part of the melted PCM at 318.15 K and maintained a fairly constant L_f value of around 0.4 at 313.15 K.

$\overline{Nu}_{Battery}$ at different ambient temperatures is demonstrated in Fig. 18. At the low ambient temperature of 303.15 K, where the PCM remains unmelted and the battery surface temperature stays below the PCM melting temperature, $\overline{Nu}_{Battery}$ increased steadily during the discharge process. When the ambient temperature increased to 308.15 K, $\overline{Nu}_{Battery}$ reached a peak as the surface temperature approached the PCM solidus temperature. Once the PCM begins to melt, the thermal buffering effect of the phase change, combined with continued convective heat removal, leads to a reduction in $\overline{Nu}_{Battery}$, which decreases to approximately 135 by 720 s. At higher ambient temperatures, where the battery surface temperature exceeded the PCM solidus temperature at the start of the discharge, $\overline{Nu}_{Battery}$ exhibited a smoother trend throughout the discharge process. For the ambient temperature of 313.15 K, by 500 s, it stabilised around 40.8 and remained relatively steady until the end of discharge. This behaviour is attributed to the balance between the heat conducted

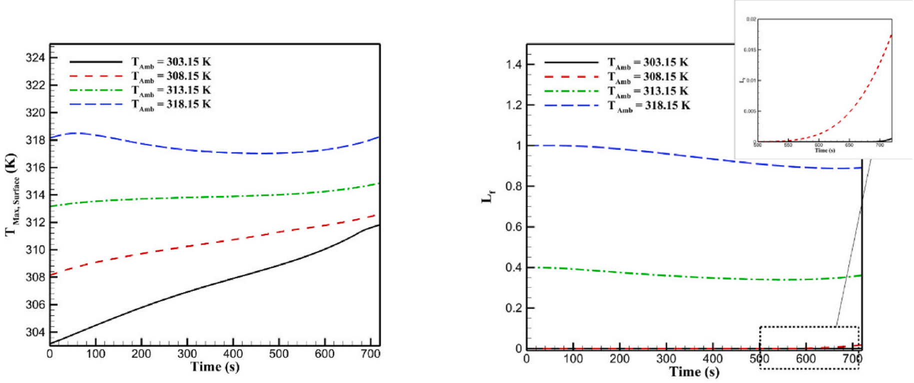

(a) (b)

Fig. 16. Impact of the ambient temperature on (a) batteries maximum surface temperature and (b) PCM liquid fraction.

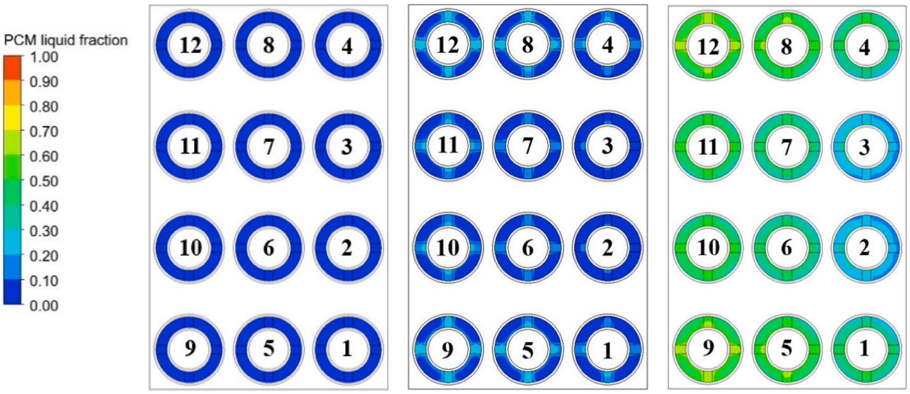

(a) T_{Amb} = 303.15 K (b) T_{Amb} = 308.15 K (c) T_{Amb} = 313.15 K

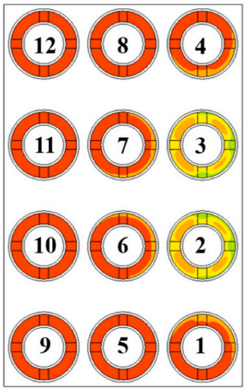

(d) T_{Amb} = 318.15 K

Fig. 17. PCM liquid fraction contour plots at different ambient temperatures at the 720 s.

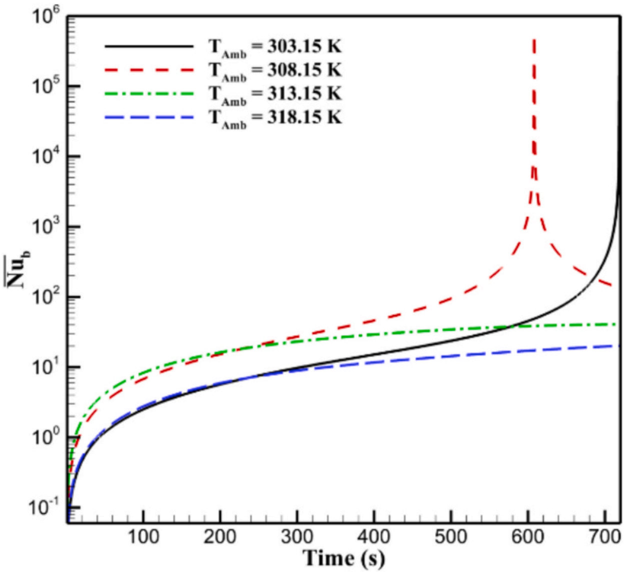

Fig. 18. Batteries surface average Nusselt number for HBTMS at different ambient temperatures at 720 s.

through the battery housing into the PCM, fins, PCM housing, and cooling plates, and the heat removed by convection in the copper tubes enhanced by the metal foam layers. As shown in Fig. 16 (b), this balance is reflected in the consistently constant L_f value during discharge. At the highest ambient temperature of 318.15 K, a similar trend was observed, with $\overline{Nu}_{Battery}$ exhibiting a quasi-steady behaviour during the last 20 s of discharge, reaching a value of approximately 20.2.

Each battery's $T_{Max,\ Surface}$ and $\Delta T_{Max,\ Surface}$ at different ambient temperatures is presented in Fig. 19. As the ambient temperature increased, higher $T_{Max,\ Surface}$ values were observed with a consistent pattern of the highest temperatures occurring on batteries 9 and 12 and the lowest on batteries 2 and 3. $\Delta T_{Max,\ Surface}$ also had an increasing trend with higher ambient temperatures, with the highest $\Delta T_{Max,\ Surface}$ value on battery 4. When comparing ambient temperatures of 303.15 K and 308.15 K, a reduction of about 28 % in $\Delta T_{Max,\ Surface}$ was observed at 308.15 K, attributed to increased PCM melting in metal foam fins, which absorbs a greater fraction of the heat generated by the battery. At higher ambient temperatures of 313.15 and 318.15, $\Delta T_{Max,\ Surface}$ on battery 4 reached about 1 K and 1.2 K, respectively, both values are well below the critical 5 K threshold. The maximum temperature differences among the batteries in the pack were 1.3 K, 1.27 K, 2.1 K, and 3.43 K for ambient temperatures of 303.15 K, 308.15 K, 313.15 K, and 318.15 K, respectively, which is also below the 5 K threshold. These findings emphasise that the integration of PCM with longitudinal metal foam fins and cooling plates with copper tubes enhanced by metal foam layers effectively controls the maximum temperature while ensuring a uniform and acceptable temperature distribution within the battery pack even at high ambient temperatures.

5. Conclusion

Effective thermal management systems are crucial for enhancing the performance, safety, and lifespan of lithium-ion batteries (LIBs). Therefore, this study numerically investigated a hybrid battery thermal management system (HBTMS) that integrates phase change material (PCM), copper metal foam as longitudinal fins and metal foam layers, along with liquid cooling. Unlike previous studies that typically adopt

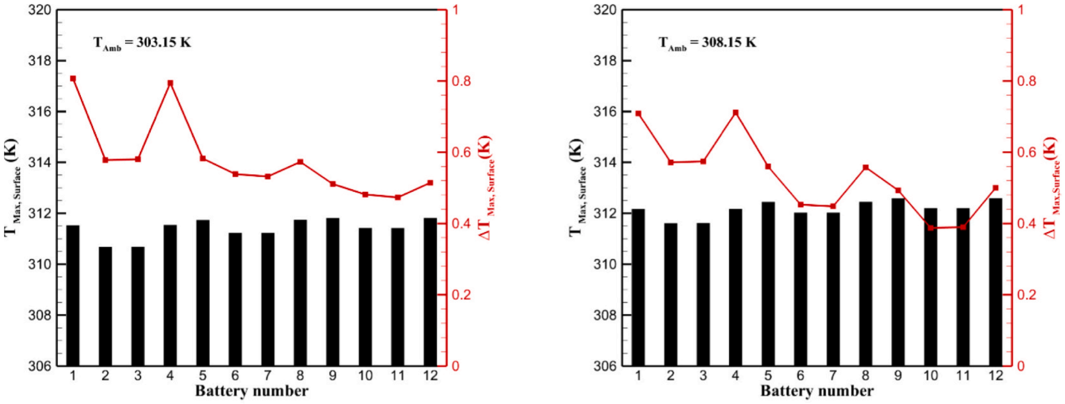

(a) T_{Amb} = 303.15 K (b) T_{Amb} = 308.15 K

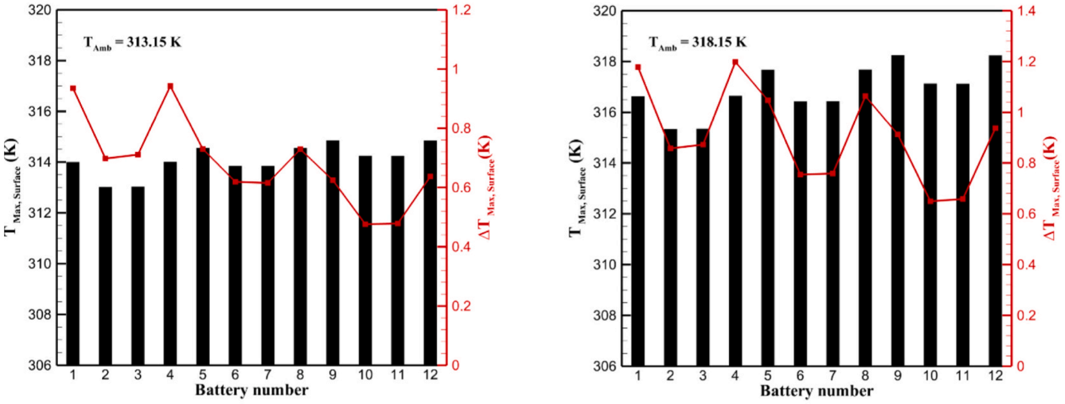

(c) T_{Amb} = 313.15 K (d) T_{Amb} = 318.15 K

Fig. 19. Comparison of the $T_{Max,\ Surface}$ and $\Delta T_{Max,\ Surface}$ of the HBTMS at different ambient temperatures at 720 s.

conventional solid fins or address passive and active cooling separately, this work addresses an important gap by optimising the use of metal foam fins and layers within the HBTMS. The system achieves substantial enhancements in thermal performance and energy density due to the unique structure of metal foam, characterised by its interconnected pores, which facilitate heat conduction in the PCM and enhance convective heat transfer in the liquid cooling system. The effects of critical parameters, including the number of cooling plates with or without metal foam layer, the thickness of the metal foam layer within the copper tube, and the ambient temperature, were thoroughly analysed to evaluate their influence on the thermal and design performance of the HBTMS. The conclusions drawn from the study are as follows:

1. Enhanced thermal management:
   - By incorporating the HBTMS with cooling plates and copper metal foam the maximum battery surface temperature was reduced by up to 9.68 K, compared to pure PCM cooling.
   - At high ambient temperatures, the system delayed PCM melting and limited the maximum surface temperature rise, enhancing performance consistency.
2. Optimised metal foam integration:
   - Metal foam layer with 4 mm thickness in the copper tube was identified as optimal, providing the best balance between improved heat transfer and minimal pressure drop, with performance evaluation criteria (PEC) of 1.41, indicating enhanced thermal performance relative to pressure drop compared to clear copper tube.
   - Fully filling the copper tubes hindered convection and reduced overall performance, emphasising the advantages of partially filled designs.
   - The inclusion of metal foam layers in the cooling tubes reduced the PCM liquid fraction by up to 97.51 % in HBTMS with three cooling plates.
3. Improved energy density:
   - The optimised HBTMS design achieved a similar thermal performance with fewer cooling plates, demonstrating an 11 % improvement in energy density.
4. Uniform temperature distribution:
   - Across all scenarios, the temperature gradient within the battery pack and each individual cell remained well below the critical threshold of 5 K, ensuring uniformity.

CRediT authorship contribution statement

Alireza Keyhani-Asl: Writing – review & editing, Writing – original draft, Visualization, Validation, Software, Methodology, Investigation, Formal analysis. **Noel Perera:** Writing – review & editing, Supervision, Project administration. **Jens Lahr:** Supervision. **Reaz Hasan:** Writing – review & editing, Supervision, Conceptualization.

Funding

This research did not receive any specific grant from funding agencies in the public, commercial, or not-for-profit sectors.

Declaration of competing interest

The authors declare that they have no known competing financial interests or personal relationships that could have appeared to influence the work reported in this paper.

Acknowledgments

The authors express their sincere appreciation to Dr Roger Tait for his invaluable guidance and advice in the use of the HPC (Cluster 3) resource. They also extend their gratitude to the Faculty of Computing, Engineering, and the Built Environment at Birmingham City University for their support in facilitating access to this resource.

Data availability

Data will be made available on request.

References

[1] X. Zhang, Z. Li, L. Luo, Y. Fan, Z. Du, *A review on thermal management of lithium-ion batteries for electric vehicles*, Energy 238 (2022) 121652.

[2] K. Liu, K. Li, Q. Peng, C. Zhang, *A brief review on key technologies in the battery management system of electric vehicles*, Front. Mech. Eng. 14 (1) (2019) 47–64.

[3] M. Al-Zareer, I. Dincer, M.A. Rosen, *A review of novel thermal management systems for batteries*, Int. J. Energy Res. 42 (10) (2018) 3182–3205.

[4] J. Jaguemont, L. Boulon, Y. Dube, F. Martel, *Thermal management of a hybrid electric vehicle in cold weather*, IEEE Trans. Energy Convers. 31 (3) (2016) 1110–1120.

[5] Z. Lei, Z. Maotao, X. Xiaoming, G. Junkui, *Thermal runaway characteristics on NCM lithium-ion batteries triggered by local heating under different heat dissipation conditions*, Appl. Therm. Eng. 159 (2019) 113847.

[6] P. Ramadass, B. Haran, R. White, B.N. Popov, *Capacity fade of Sony 18650 cells cycled at elevated temperatures: Part I. Cycling performance*, J. Power Sources 112 (2) (2002) 606–613.

[7] A. Angani, H.-W. Kim, M.-H. Hwang, E. Kim, K.-M. Kim, H.-R. Cha, *A comparison between Zig-Zag plated hybrid parallel pipe and liquid cooling battery thermal management systems for Lithium-ion battery module*, Appl. Therm. Eng. 219 (2023) 119599.

[8] P.G. Zadeh, Y. Wang, J.D. Chung, *Thermal management modeling for cylindrical lithium-ion battery packs considering safety and lifespan*, J. Mech. Sci. Technol. 36 (7) (2022) 3727–3733.

[9] W. Wu, S. Wang, W. Wu, K. Chen, S. Hong, Y. Lai, *A critical review of battery thermal performance and liquid based battery thermal management*, Energ. Conver. Manage. 182 (2019) 262–281.

[10] P. Zare, N. Perera, J. Lahr, R. Hasan, *Solid-liquid phase change materials for the battery thermal management systems in electric vehicles and hybrid electric vehicles–a systematic review*, J. Storage Mater. 52 (2022) 105026.

[11] Z. Rao, Z. Qian, Y. Kuang, Y. Li, *Thermal performance of liquid cooling based thermal management system for cylindrical lithium-ion battery module with variable contact surface*, Appl. Therm. Eng. 123 (2017) 1514–1522.

[12] Z. Ling, F. Wang, X. Fang, X. Gao, Z. Zhang, *A hybrid thermal management system for lithium ion batteries combining phase change materials with forced-air cooling*, Appl. Energy 148 (2015) 403–409.

[13] P. Zare, N. Perera, J. Lahr, R. Hasan, *A novel thermal management system for cylindrical lithium-ion batteries using internal-external fin-enhanced phase change material*, Appl. Therm. Eng. 238 (2024) 121985.

[14] P. Zare, N. Perera, J. Lahr, R. Hasan, *Uniform temperature distribution, prolonged temperature regulation, and accelerated recovery of battery thermal management system using a novel fin design*, J. Storage Mater. 108 (2025) 115054.

[15] A. Keyhani-Asl, N. Perera, J. Lahr, R. Hasan, *Porous media and foam application in battery thermal management systems: a comprehensive review focused on its impact, numerical modeling, and experimental preparation*, J. Storage Mater. 93 (2024) 112306.

[16] K. Jiang, G. Liao, E. Jiaqiang, F. Zhang, J. Chen, E. Leng, *Thermal management technology of power lithium-ion batteries based on the phase transition of materials: a review*, J. Storage Mater. 32 (2020) 101816.

[17] Z. Sun, Y. Guo, C. Zhang, J. Whitehouse, Q. Zhou, H. Xu, C. Wang, *Experimental study of battery passive thermal management system using copper foam-based phase change materials*, Int. J. Thermofluids 17 (2023) 100255.

[18] J.T. Rajan, V.S. Jayapal, M. Krishna, K.M. Firose, S. Vaisakh, A.K. John, A. Suryan, *Analysis of battery thermal management system for electric vehicles using 1-Tetradecanol phase change material*, Sustainable Energy Technol. Assess. 51 (2022) 101943.

[19] B. Buonomo, O. Manca, F. Menale, S. Nardini, *Numerical investigation on the thermal control of lithium batteries for electric cars using metal foams and phase change materials. Journal of Physics: Conference Series*, IOP Publishing, 2021.

[20] M.M. el Idi, M. Karkri, M.A. Tankari, S. Vincent, *Hybrid cooling based battery thermal management using composite phase change materials and forced convection*, J. Storage Mater. 41 (2021) 102946.

[21] M.M. El Idi, M. Karkri, M.A. Tankari, *A passive thermal management system of Li-ion batteries using PCM composites: Experimental and numerical investigations*, Int. J. Heat Mass Transf. 169 (2021) 120894.

[22] J. Lin, D. Liu, X. Liu, M. Liu, Y. Cui, *CNT@ MXene porous composite PCM based thermal management for lithium-ion battery system*, Appl. Therm. Eng. 262 (2025) 125240.

[23] B. Li, L. Zhang, B. Shang, Y. Huo, *Numerical investigation on heat transfer characteristics in battery thermal management with phase change material composited by toroidal porous medium*, Int. Commun. Heat Mass Transfer 154 (2024) 107414.

[24] D.A. Nield, A. Bejan, *Convection in porous media*. Vol. 3. 2006: Springer.

[25] S. Ki, J. Lee, S. Kim, J. Seong, J. Shim, S. Oh, S. Cho, S. Bang, D. Seo, J. Kim, *An energy-efficient battery thermal management system incorporating a porous metal-based multiscale flow manifold*, Energ. Conver. Manage. 269 (2022) 116147.

[26] J. Xu, Z. Guo, Z. Xu, X. Zhou, X. Mei, *A systematic review and comparison of liquid-based cooling system for lithium-ion batteries*, eTransportation (2023) 100242.

[27] X. Du, Z. Wang, Q. Gao, H. Yang, R. Bao, S. Xiong, *Study on novel battery thermal management using triply periodic minimal surface porous structures liquid cooling channel*, Appl. Therm. Eng. 257 (2024) 124384.

[28] M. Rabiei, A. Gharehghani, A.M. Andwari, *Enhancement of battery thermal management system using a novel structure of hybrid liquid cold plate*, Appl. Therm. Eng. (2023) 121051.

[29] W. Jiang, G. Feng, H. Wang, Z. Chang, X. Tan, J. Ji, Y. Zhang, J. Zhou, *Analysis of hybrid active-passive prismatic Li-ion battery thermal management system using phase change materials with porous-filled mini-channels*, J. Storage Mater. 80 (2024) 110144.

[30] J. Jongpluempiti, P. Vengsungnle, S. Poojeera, S. Eiamsa-ard, N. Naphon, A. Srichat, K. Manatura, P. Naphon, *Thermal profile analysis of 18659 Li-ion battery module with embedded copper foam in the nanofluid cooling jacket*, Case Stud. Chem. Environ. Eng. (2025) 101208.

[31] B.M. Ningegowda, N. Kumar, A. Munirathinam, Pachpute, S., & Veetil, P. K. P., *An efficient immersion cooling of lithium-ion battery for electric vehicles*. In AIP Conference Proceedings (Vol. 3192, No. 1, p. 020018) 2024, November. AIP Publishing LLC.

[32] M. Bamdezh, G. Molaeimanesh, *The path from conventional battery thermal management systems to hybrid battery thermal management systems for electric vehicles, opportunities and challenges*, J. Storage Mater. 100 (2024) 113160.

[33] J.R. Patel, M.K. Rathod, *Recent developments in the passive and hybrid thermal management techniques of lithium-ion batteries*, J. Power Sources 480 (2020) 228820.

[34] M. Waseem, M. Ahmad, A. Parveen, M. Suhaib, *Battery technologies and functionality of battery management system for EVs: current status, key challenges, and future prospectives*, J. Power Sources 580 (2023) 233349.

[35] H.N. Khaboshan, F. Jaliliantabar, A.A. Abdullah, S. Panchal, *Improving the cooling performance of cylindrical lithium-ion battery using three passive methods in a battery thermal management system*, Appl. Therm. Eng. 227 (2023) 120320.

[36] H. Liu, S. Ahmad, Y. Shi, J. Zhao, *A parametric study of a hybrid battery thermal management system that couples PCM/copper foam composite with helical liquid channel cooling*, Energy 231 (2021) 120869.

[37] Y. Zhao, B. Zou, C. Li, Y. Ding, *Active cooling based battery thermal management using composite phase change materials*, Energy Procedia 158 (2019) 4933–4940.

[38] M. Mashayekhi, E. Houshfar, M. Ashjaee, *Development of hybrid cooling method with PCM and Al2O3 nanofluid in aluminium minichannels using heat source model of Li-ion batteries*, Appl. Therm. Eng. 178 (2020) 115543.

[39] H. Yang, Z. Wang, R. Bao, B. Zhang, X. Zhu, H. Wang, *A novel hybrid battery thermal management system using TPMS structure and delayed cooling scheme*, Appl. Therm. Eng. 259 (2025) 124901.

[40] A. Keyhani-Asl, N. Perera, J. Lahr, R. Hasan, *Innovative hybrid battery thermal management system incorporating copper foam porous fins and layers with phase change material and liquid cooling*, Appl. Therm. Eng. (2025) 125848.

[41] P. Jindal, R. Katiyar, J. Bhattacharya, *Evaluation of accuracy for Bernardi equation in estimating heat generation rate for continuous and pulse-discharge protocols in LFP and NMC based Li-ion batteries*, Appl. Therm. Eng. 201 (2022) 117794.

[42] Y. Miao, P. Hynan, A. Von Jouanne, A. Yokochi, *Current Li-ion battery technologies in electric vehicles and opportunities for advancements*, Energies 12 (6) (2019) 1074.

[43] E. Jiaqiang, M. Yue, J. Chen, H. Zhu, Y. Deng, Y. Zhu, F. Zhang, M. Wen, B. Zhang, S. Kang, *Effects of the different air cooling strategies on cooling performance of a lithium-ion battery module with baffle*, Appl. Therm. Eng. 144 (2018) 231–241.

[44] P. Taheri, M. Yazdanpour, M. Bahrami, *Transient three-dimensional thermal model for batteries with thin electrodes*, J. Power Sources 243 (2013) 280–289.

[45] S. Ambekar, P. Rath, A. Bhattacharya, *A novel PCM and TCE based thermal management of battery module*, Therm. Sci. Eng. Prog. 29 (2022) 101196.

[46] Y. Lai, W. Wu, K. Chen, S. Wang, C. Xin, *A compact and lightweight liquid-cooled thermal management solution for cylindrical lithium-ion power battery pack*, Int. J. Heat Mass Transf. 144 (2019) 118581.

[47] C. Zhao, W. Cao, T. Dong, F. Jiang, *Thermal behavior study of discharging/charging cylindrical lithium-ion battery module cooled by channeled liquid flow*, Int. J. Heat Mass Transf. 120 (2018) 751–762.

[48] M. Fadl, P.C. Eames, *Numerical investigation of the influence of mushy zone parameter Amush on heat transfer characteristics in vertically and horizontally oriented thermal energy storage systems*, Appl. Therm. Eng. 151 (2019) 90–99.

[49] M. Bamdezh, G. Molaeimanesh, S. Zanganeh, *Role of foam anisotropy used in the phase-change composite material for the hybrid thermal management system of lithium-ion battery*, J. Storage Mater. 32 (2020) 101778.

[50] J.M. Mahdi, E.C. Nsofor, *Melting enhancement in triplex-tube latent heat energy storage system using nanoparticles-metal foam combination*, Appl. Energy 191 (2017) 22–34.

[51] P. Wang, X. Wang, Y. Huang, C. Li, Z. Peng, Y. Ding, *Thermal energy charging behaviour of a heat exchange device with a zigzag plate configuration containing multi-phase-change-materials (m-PCMs)*, Appl. Energy 142 (2015) 328–336.

[52] F. Zhang, F. Lu, B. Liang, Y. Zhu, H. Gou, K. Xiao, Y. He, *Thermal performance analysis of a new type of branch-fin enhanced battery thermal management PCM module*, Renew. Energy 206 (2023) 1049–1063.

[53] M. Maerefat, S.Y. Mahmoudi, K. Mazaheri, *Numerical simulation of forced convection enhancement in a pipe by porous inserts*, Heat Transfer Eng. 32 (1) (2011) 45–56.

[54] D. Hacen, A. Boughamoura, S.B. Nasrallah, *Forced pulsating flow and heat transfer in a tube partially filled with a porous medium*, J. Porous Media 9 (1) (2006).

[55] A.A. Al-Abidi, S. Mat, K. Sopian, M. Sulaiman, A.T. Mohammad, *Internal and external fin heat transfer enhancement technique for latent heat thermal energy storage in triplex tube heat exchangers*, Appl. Therm. Eng. 53 (1) (2013) 147–156.

[56] Y. Tian, C.-Y. Zhao, *A numerical investigation of heat transfer in phase change materials (PCMs) embedded in porous metals*, Energy 36 (9) (2011) 5539–5546.

[57] J.G. Fourie, J.P. Du Plessis, *Pressure drop modelling in cellular metallic foams*, Chem. Eng. Sci. 57 (14) (2002) 2781–2789.

[58] X. Yang, T.J. Lu, T. Kim, *An analytical model for permeability of isotropic porous media*, Phys. Lett. A 378 (30–31) (2014) 2308–2311.

[59] Z. Liu, Y. Yao, H. Wu, *Numerical modeling for solid–liquid phase change phenomena in porous media: Shell-and-tube type latent heat thermal energy storage*, Appl. Energy 112 (2013) 1222–1232.

[60] B. Alazmi, K. Vafai, *Constant wall heat flux boundary conditions in porous media under local thermal non-equilibrium conditions*, Int. J. Heat Mass Transf. 45 (15) (2002) 3071–3087.

[61] V.V. Calmidi,, R.L. Mahajan, *The effective thermal conductivity of high porosity fibrous metal foams.* 1999.

[62] V.V. Calmidi, R.L. Mahajan, *Forced convection in high porosity metal foams*, J. Heat Transfer 122 (3) (2000) 557–565.

[63] C.-C. Chen, P.-C. Huang, H.-Y. Hwang, *Enhanced forced convective cooling of heat sources by metal-foam porous layers*, Int. J. Heat Mass Transf. 58 (1–2) (2013) 356–373.

[64] A. Amiri, K. Vafai, *Analysis of dispersion effects and non-thermal equilibrium, non-Darcian, variable porosity incompressible flow through porous media*, Int. J. Heat Mass Transf. 37 (6) (1994) 939–954.

[65] A. Amiri, K. Vafai, T. Kuzay, *Effects of boundary conditions on non-Darcian heat transfer through porous media and experimental comparisons*, Numer. Heat Transf. A Appl. 27 (6) (1995) 651–664.

[66] F.P. Incropera, D.P. DeWitt, T.L. Bergman, A.S. Lavine, Fundamentals of Heat and Mass Transfer, Vol. 6, Wiley, New York, 1996.

[67] H. Xu, Z. Qu, W. Tao, *Analytical solution of forced convective heat transfer in tubes partially filled with metallic foam using the two-equation model*, Int. J. Heat Mass Transf. 54 (17–18) (2011) 3846–3855.

[68] M.A. Vatanparast, S. Hossainpour, A. Keyhani-Asl, S. Forouzi, *Numerical investigation of total entropy generation in a rectangular channel with staggered semi-porous fins*, Int. Commun. Heat Mass Transfer 111 (2020) 104446.

[69] A. Keyhani-Asl, S. Hossainpour, M. Rashidi, M.A. Sheremet, Z. Yang, *Comprehensive investigation of solid and porous fins influence on natural convection in an inclined rectangular enclosure*, Int. J. Heat Mass Transf. 133 (2019) 729–744.

[70] A. Kheradmand-Laleh, S. Hossainpour, A. Keyhani-Asl, M.A. Vatanparast, *Effect of utilizing staggered semi-porous fins on channel flow heat transfer enhancement*, Heat Transfer Eng. 44 (14) (2023) 1244–1261.

[71] Y. Mahmoudi, N. Karimi, *Numerical investigation of heat transfer enhancement in a pipe partially filled with a porous material under local thermal non-equilibrium condition*, Int. J. Heat Mass Transf. 68 (2014) 161–173.

[72] P.J. Roache, *Perspective: a method for uniform reporting of grid refinement studies,* 1994.

[73] Division, A.S.o.M.E.F.E., *Quantification of Uncertainty in Computational Fluid Dynamics*. 1993: American Society of Mechanical Engineers.

[74] R. Oliveira, G. Justi, G. Lopes, *Grid convergence study of a cyclone separator using different mesh structures*, Chem. Ind. Chem. Eng. Q. 23 (3) (2017) 311–320.

[75] X. Hu, F. Zhu, X. Gong, *Experimental and numerical study on the thermal behavior of phase change material infiltrated in low porosity metal foam*, J. Storage Mater. 26 (2019) 101005.

[76] M. Amani, M. Ameri, A. Kasaeian, *The experimental study of convection heat transfer characteristics and pressure drop of magnetite nanofluid in a porous metal foam tube*, Transp. Porous Media 116 (2017) 959–974.

[77] L.-L. Tian, X. Liu, S. Chen, Z.-G. Shen, *Effect of fin material on PCM melting in a rectangular enclosure*, Appl. Therm. Eng. 167 (2020) 114764.

[78] M. Torabi, K. Zhang, G. Yang, J. Wang, P. Wu, *Heat transfer and entropy generation analyses in a channel partially filled with porous media using local thermal non-equilibrium model*, Energy 82 (2015) 922–938.

[79] A. Greco, X. Jiang, D. Cao, *An investigation of lithium-ion battery thermal management using paraffin/porous-graphite-matrix composite*, J. Power Sources 278 (2015) 50–68.

[80] J. Zhang, X. Li, G. Zhang, H. Wu, Z. Rao, J. Guo, D. Zhou, *Experimental investigation of the flame retardant and form-stable composite phase change materials for a power battery thermal management system*, J. Power Sources 480 (2020) 229116.

[81] M.A. Teamah, W.M. El-Maghlany, M.M.K. Dawood, *Numerical simulation of laminar forced convection in horizontal pipe partially or completely filled with porous material*, Int. J. Therm. Sci. 50 (8) (2011) 1512–1522.

[82] W. Lu, T. Zhang, M. Yang, *Analytical solution of forced convective heat transfer in parallel-plate channel partially filled with metallic foams*, Int. J. Heat Mass Transf. 100 (2016) 718–727.

[83] M.E. Nimvari, M. Maerefat, M. El-Hossaini, *Numerical simulation of turbulent flow and heat transfer in a channel partially filled with a porous media*, Int. J. Therm. Sci. 60 (2012) 131–141.

[84] S.K. Saha, H. Ranjan, M.S. Emani, A.K. Bharti, *Performance Evaluation Criteria in Heat Transfer Enhancement*, Springer, 2020.